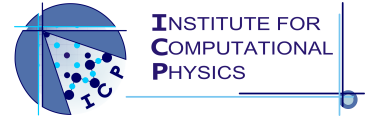**Universität Stuttgart**

Master Thesis

Physical and geometric characterization of stochastic interfaces for the case of Bentheimer sandstone

Samer Afach

October 3, 2010

Institute for Computational Physics

Table of contents

Acknowledgments

I would like to express my deep felt gratitude to my advisor, Thomas Zauner, for his advice, encouragement, enduring patience and constant support; he was always providing clear explanations when I was lost, and always giving me the first step for brilliant solutions to problems I always have faced and always giving me his time, in spite of anything else that was going on. His response to my verbal thanks is very modest as "It's my job".

And I wish also to thank my colleagues in the institute, especially, Oliver Hönig, Florian Dommert, Rudolf Weeber, Stefan Kesselheim and Florian Rühle for the nice and friendly atmosphere they offered me while I was doing my thesis, and for their kind help and support with their fast answers and explanations that saved me from wasting long hours of searching, and for their great efforts and patience for improving my German language skills which was a great and important part of my life in Germany.

And I would like to thank my Supervisor Prof. Rudolf Hilfer for the great support; his small advices taught me so much about working in an academic atmosphere, and in solving problems systematically and scientifically. I admit that his small and simple explanations revealed to me how much I still have to learn to become a real scientist like him who has a really big amount of knowledge that he transfers in small and meaningful words to the new students and scientists who still have a long way on their path of the life of science.

And I must thank my friend and brother Basel Darwich, who was a close buddy and advisor for my life in the whole path of my thesis; as he studies medicine and has nothing to do with physics, he always listened neutrally to my arguments of my thesis work with great patience and made me learn and improve the way I deliver information to a reader and listener in its simplest form.

And finally, the real thanks go to my mother and family for their great support for my life in Germany and for encouraging me to travel to learn since my childhood, and for offering me the family atmosphere despite the distance between us.

1. Introduction

Motivation

Porous media have been a concern since the 60s; the main challenge has been about how the connection between the microstructure and the macroscopic properties is formed, and what the attributes and characteristics are that define their microstructure. In general, this problem has been already investigated in what is called *disordered systems*; the crystallites making up the subject-materials are arranged randomly in space. Examples to other recent studies done on disordered systems could be found in [13, 37, 29]. Our study, using techniques of theoretical and computational physics, highlights finding the regularities in stochastic porous media that can be put together to obtain generated porous media using statistical mechanics and disordered systems concepts.

Objective and problem definition

The main question of many physics problems applies in this thesis as well; how do the microstructure's characteristics affect the macrostructure's physical quantities. In [24], the microstructure of a porous medium was given a quantitative characterization through porosity, specific surface, two-point correlation function, local porosity theory (LPT) and others. The microstructure characteristics were used there after to characterize some porous media and build models for them, and to assess whether the models fit the experimental sample. In [3] a laboratory scale multiscale carbonate rock was modeled using a continuum geometrical modeling technique and transport properties were successfully predicted. A good match was achieved between the model and the experimental sample. In [31] the same approach was utilized to model the Fontainebleau sandstone with a side-length 1.5 cm. From what we have seen in previous work, to create a convenient model, the points we need to answer are as follows

- What is the right way to segment the contents of the experimental sample, since the microstructure characteristics are strongly dependent on the gray-scale level chosen to discriminate between solids and voids [9]?

- Does the current modeling approach suffice for modeling every sandstone? does it need improvement?

- What are the modeling parameters that we have to tweak in order to control a certain microstructure characteristic? and how?

- Would the transport properties of a model agree with an experimental sample if they both match qualitatively and quantitatively by their microstructure's characteristics?

In this thesis I concentrate on modeling one kind of porous media and studying its microstructure's characteristics; this porous medium is the sandstone called Bentheimer. I start in Chapter 2 by defining the microstructure parameters and statistical physics concepts that I will be using. Then in Chapter 3 I analyze the Bentheimer's μ-CT (Computerized microtomography) images to evaluate the microstructure characteristics. In Chapter 4 the physics concepts and computational techniques that I will be using to build the model are discussed. In Chapter 5 I study the modeling parameters that are discussed in Chapter 4, and try to understand the tend of these parameters and their effect on the model's microstructure characteristics. Finally, in Chapter 6, I present the model that I have chosen to be the Bentheimer model according to what is learned from Chapter 5, and show Lattice Boltzmann simulations' results that are applied on the experimental sample and the model, and see whether they agree in transport properties, especially, permeability.

2. Theoretical introduction

2.1. Porous media

A porous medium or material is a solid that contains an interconnected pores network. The solid that surrounds these pores is often called "matrix". Porosity is an important attribute of many materials; it is a measure of the rock's potential in storing economically important fluids like oil or water. Some examples of common porous media in our life are rocks, soils, biological tissues and ceramics. Porosity is also important because it contributes to many physical properties like density, specific conductance and dielectric constant.

Porosity

Porosity, called often voidage, is the fraction of the pore volume to the total volume. There are two types of pore spaces. The first type forms a continuous phase within the porous medium; i.e., allows fluids flow though the porous medium. Those pores are called "interconnected" or "effective" pores. The second type is the opposite, where we find pores closed to themselves (isolated or non-interconnected). The latter cannot contribute to matter transport across the porous medium.

   Later, we will define porosity in a more elaborated sense according to our mathematical definition of porous media.

2.2. Mathematical definition of porous media

An n-component porous medium is defined as a compact and singly connected subset $\mathbb{S}$ of $\mathbb{R}^d$, which contains n closed subsets $\mathbb{P}_i \in \mathbb{S}$ so that [24, P. 307]

$$
\begin{align}
\mathbb{S} &= \mathbb{P}_1 \cup \cdots \cup \mathbb{P}_n, \tag{2.2.1} \\
0 &= V_d(\partial \mathbb{P}_i), \tag{2.2.2}
\end{align}
$$

for $1 \leqslant i \leqslant n$. $\mathbb{S}$ is called sample space, which may represent in general any porous medium, $\mathbb{P}$ represent different phases or components of the sample. Such as different materials in a rock. The symbol $V_d(G)$ denotes the d-dimensional volume of a set $G \subset R$, which we define as follows [24, P. 308]

$$
V_d(G) = \int \chi_G(\vec{r}) \, d^d \vec{r}, \tag{2.2.3}
$$

where $\vec{r}$ is a d-dimensional vector, and $d^d\vec{r}$ is the d-dimensional Lebesgue volume measure. In Eq. (2.2.3), the function $\chi_G(\vec{r})$ is called the characteristic function of the sample. It indicates

whether the point referred to by the vector $\vec{r}$ is an element of G [24, P. 308], i.e.,

$$\chi_G(\vec{r}) = \begin{cases} 1 & \text{for } \vec{r} \in G \\ 0 & \text{for } \vec{r} \notin G. \end{cases} \tag{2.2.4}$$

The symbol (or operator) ∂ before a volume element denotes the boundaries of the volume element, so we mean with $\partial\mathbb{P}_i$ the boundary of the component i in the porous medium, so if the system is 3-dimensional, $\partial\mathbb{P}_i$ would give the surface that surrounds the component i.

The different components or phases of the sample may consist of fluid phases and solid phases. It is convenient to point to the solid phases collectively as a *matrix space* $\mathbb{M}$, and other phases are denoted as *pore space* $\mathbb{P}$. With this convention we may redefine the sample as the union of the matrix and pore phases $\mathbb{S} = \mathbb{M} \cup \mathbb{P}$. We define also the intersection between the matrix phase and the pore phase as the surface boundary between the two phases $\mathbb{P} \cap \mathbb{M} = \partial\mathbb{P} = \partial\mathbb{M}$ [24, P. 310].

2.3. Stochastic geometry implication

The geometry of porous media appears usually to be random or to have random characteristics, this suggests the use of probabilistic methods for modeling. The idealization underlying the use of statistical methods is that the geometry of the porous medium is a realization drawn at random from an ensemble of possible geometries. This idealization involves discussing ensembles rather than individual geometries. It assumes that there exists some form of recognizable statistical regularity in the fluctuations and heterogeneities of the microstructure. This idealization is modeled after statistical mechanics where the microstructure corresponds to a full specification of the positions and momenta of the particles in a fluid while the regularities are contained in the equation of state or thermodynamic potentials. These regularities of the porous media can be described by a suitable probability distribution on the space of all geometries. The merit of the stochastic description lies in the fact that it defines the necessary framework to define typical or average properties of porous media [24, P. 312].

We distinguish here between two concepts, stationarity (homogeneity) and heterogeneity. Most porous media are heterogeneous, meaning that there does not exist a large length-scale limit where the geometrical and physical properties stop fluctuating upon increasing the scale from microscopic to macroscopic. Stationarity (homogeneity) assumes the existence of such a scale, beyond which fluctuations decrease [2, 24].

2.3.1. Discrete space

Consider a cubic porous sample with side-length L, and let a be the macroscopic resolution. With this, there are then $N = \left(\frac{L}{a}\right)^d$ non-overlapping volume elements in the sample that could be addressed by their position vectors [24, P. 313]

$$\vec{r}_i = \vec{r}_{i_1 \cdots i_d} = (ai_1, \ldots, ai_d), \tag{2.3.1}$$

where the integers $1 \leqslant i_1, \cdots, i_d \leqslant \frac{L}{a}$, and $\vec{r}_i$ is a shorthand notation for $\vec{r}_{i_1 \cdots i_d}$. A random configuration G of an n-component porous medium is then given as an N-tuple $G = (X_1, \ldots, X_N) = (X(\vec{r}_1), \ldots, X(\vec{r}_i))$, where the random variables $X_i \in \mathbb{I}_n = \{\rho_{\mathbb{P}_1}, \ldots, \rho_{\mathbb{P}_n}\}$ are [24, P. 313]

$$X_i = X(\vec{r}_i) = \sum_{j=1}^{n} \rho_{\mathbb{P}_j} \cdot \chi_{\mathbb{P}_j}(\vec{r}_i) \tag{2.3.2}$$

that indicate to the presence of the phase $\mathbb{P}_i$ in the volume element $\vec{r}_i$ as defined from its probability distribution $\rho_{\mathbb{P}_i}$. The set $\mathbb{I} = \{\rho_{\mathbb{P}_1}, \ldots, \rho_{\mathbb{P}_n}\}$ is a set of indicators, here the probability distributions, that are used to label every phase. The discretization of the system is chosen so that $r_i \notin \partial \mathbb{P}_j$ for all $1 \leqslant i \leqslant N$ and $1 \leqslant j \leqslant n$.

A stochastic n-component porous medium is defined as a discrete probability distribution on the set of geometries [24, P. 313]

$$\begin{aligned} \mu(x_1, \ldots, x_N) &= \Pr\{G = (x_1, \ldots, x_N)\} \\ &= \Pr\{(X_1 = x_1) \wedge \cdots \wedge (X_N = x_N)\} \end{aligned} \tag{2.3.3}$$

where $x_i \in \mathbb{I}_n = \{\rho_{\mathbb{P}_1}, \ldots, \rho_{\mathbb{P}_n}\}$. The expectation values of the functions $f(G) = f(x_1, \ldots, x_N)$ of the stochastic geometry are [24, P. 314]

$$\langle f(G) \rangle = \langle f(x_1, \ldots, x_N) \rangle = \sum_{x_1 \in \mathbb{I}_n} \cdots \sum_{x_N \in \mathbb{I}_n} f(x_1, \ldots, x_N) \mu(x_1, \ldots, x_N), \tag{2.3.4}$$

where the sum goes over every configuration in the geometry.

A stochastic porous medium is called homogeneous (stationary) if the distribution $\mu(x_1, \ldots, x_N) = \mu(x(r_1), \ldots, x(r_N))$ is translational invariant [24, P. 314], meaning

$$\mu(x(\vec{r}_1), \ldots, x(\vec{r}_N)) = \mu(x(\vec{r}_1 + \vec{q}), \ldots, x(\vec{r}_N + \vec{q})) \tag{2.3.5}$$

for all $N \in \mathbb{N}$, $\vec{q} \in \mathbb{R}$.

A stochastic porous medium is called *isotropic* if its distribution is invariant under Euclidean motions [24, P. 314], meaning

$$\mu(x(\vec{r}_1), \ldots, x(\vec{r}_N)) = \mu\left(x\left(\overleftrightarrow{R} \cdot \vec{r}_1\right), \ldots, x\left(\overleftrightarrow{R} \cdot \vec{r}_N\right)\right) \tag{2.3.6}$$

for all $N \in \mathbb{N}$, where $\overleftrightarrow{R}$ refers to an operator that consists of a translation and rotation.

The possible geometries have n^N elements. For a sample with side length $L = 1\,\mathrm{cm}$ and discretized with resolution $a = 10^{-10}\,\mathrm{m}$, we find $2^{10^{24}}$ possible configurations; therefore, the probability distribution $\mu(x_1, \ldots, x_N)$ is not enough to give a complete description for all volume elements, but this does not deny the theoretical importance of the microscopic distribution $\mu(x_1, \ldots, x_N)$. It is in fact more useful to generalize it to continuous space where infinite amount of data is required to specify the distribution [24].

2.3.2. Continuous space

Rather than discretizing the space, we could work with random sets in continuous space. Literature for random sets are [33, 28], and more details in [24].

In order to define random sets, recall probability space and random variables [38, 10, 11]. In probabilities theory, an event $\mathbb{E}$ is a subset of a set $\mathbb{O}$ that represents all possible outcomes of a random experiment. The probability of an event $\Pr(\mathbb{E})$ is a set function that obeys the basic rules $\Pr(\mathbb{O}){=}1$ and $\Pr(\mathbb{E}) \geqslant 0$ and $\Pr(\cup_{i=1}^{\infty}\mathbb{E}_i) = \sum_{i=1}^{\infty} \Pr(\mathbb{E}_i)$ where $\mathbb{E}_i \cap \mathbb{E}_j = \emptyset$ if $i \neq j$. We define the conditional probability of an event $\mathbb{E}$ given an event $\mathbb{G}$ as

$$\Pr(\mathbb{E}|\mathbb{G}) = \frac{\Pr(\mathbb{E} \cap \mathbb{G})}{\Pr(\mathbb{G})}. \tag{2.3.7}$$

Random variables are real valued functions on the probability space. Random sets are a generalization of random variables, where random sets could be understood in the same way we do with random variables with the concept "hit or miss". With this concept, it is possible to characterize a random set by intersecting it with a few arbitrary compact test sets, and recording whether the intersection is empty [33, 28]. Let $\mathcal{F}$ denote all closed sets in $\mathbb{R}^d$ including the empty set $\emptyset$, and $\mathcal{K}$ denotes all compact sets. The smallest σ-algebra $\mathfrak{F}$ of subsets of $\mathcal{F}$ which contains all the hitting sets is defined as $\mathcal{F}_{\mathbb{K}} = \{\mathbb{F} \in \mathcal{F} : \mathbb{F} \cap \mathbb{K} \neq \emptyset\}$ where $\mathbb{K}$ is a compact test set. In this context we define an event to be the statement whether a random set hits a particular countable family of subsets.

A random set $\mathbb{X}$ is defined as a measurable map from probability space $(\mathbb{O}, \mathfrak{D}, \mu)$ to $(\mathcal{F}, \mathfrak{F})$ [33]. This gives the possibility for the assignment of probabilities to countable unions and intersections of the sets $\mathcal{F}_{\mathbb{K}}$ which are the elements of $\mathfrak{F}$. For example

$$\Pr(\mathcal{F}_{\mathbb{K}}) = \mu\left(X^{-1}(\mathcal{F}_{\mathbb{K}})\right) \tag{2.3.8}$$

is the probability for the intersection $\mathbb{X} \cap \mathbb{K}$ not to be empty. This probability plays an important role in geometric characterization of porous media based on capacity functionals [33, 7, 24]. Note that there does not exist a mathematical formula for the expectation value as there is for the discrete case, in Eq. 2.3.4. Its definition that is not needed here, requires the introduction of functional integral on infinite dimensional spaces, or the study of random measures associated with random set $\mathbb{X}$ [33, 24].

The concepts of stationarity and isotropy are straightforwardly generalized as a consequence for the expectation value not being readily carried over to the continuous case. We call a random set $\mathbb{X}$ stationary if [24, P. 316]

$$\Pr\{X \cap \mathbb{K} \neq \emptyset\} = \Pr\{(\mathbb{X} + \vec{r}) \cap \mathbb{K} \neq \emptyset\} \tag{2.3.9}$$

for all vectors $\vec{r} \in \mathbb{R}^d$ and all compact sets $\mathbb{K}$. $\mathbb{G} + \vec{r}$ is a notation that denotes the *translated set* defined as [24, P. 316]

$$\mathbb{G} + \vec{r} = \{\vec{q} + \vec{r} : \vec{q} \in \mathbb{G}\} \tag{2.3.10}$$

for $\mathbb{G} \subset \mathsf{R}$ and $\vec{r} \in \mathbb{R}$. The analogous notation gives

$$\mathbb{R}\mathbb{G} = \{\mathbb{R}\vec{q} : q \in \mathbb{G}\} \tag{2.3.11}$$

for R a rigid euclidean motion, it is allowed to define an *isotropic* random set if

$$\Pr\{\mathbb{X} \cap \mathbb{K} \neq \emptyset\} = \Pr\{(\mathbb{R}\mathbb{X}) \cap \mathbb{K} \neq \emptyset\} \tag{2.3.12}$$

for all rigid motions R and compact sets $\mathbb{K}$. Later we will use the notation

$$c\mathbb{G} = \{c\vec{q} : \vec{q} \in \mathbb{G}\} \tag{2.3.13}$$

to denote the multiplication of sets by real numbers. The traditional definition of stationarity that is presented in 2.3.9 is restricted to macroscopically homogeneous porous media. The general definition of stationarity is a special case of the more general concept of *fractional stationarity* which describes macroscopic heterogeneity [18, 17, 19, 21].

The mathematical definition of random sets in continuous space is even less accessible from a practical point of view than its definition for a discretized space. A complete specification of a random set would need the specification of every compact or every closed subset of $\mathbb{R}^d$ which is practically impossible [24, P. 316].

2.4. Geometrical characterization

A complete specification of the microstructure of real porous media is not practical. In this section we discuss the possibilities to describe a porous medium without specifying all its porous geometry in details which is our main theoretical task [24, P. 316].

Characterization of porous media in general has to satisfy the following requirements [24, P. 316]:

- It should be well defined in terms of geometric quantities.

- It should involve only parameters which are directly observable or measurable in an experiment independent of the phenomenon of interest.

- It should not require the specification of too many parameters. The required independent experiments should be simple and economical to carry out. What is economical depends on the available data processing technology.

- The characterization should be usable in exact or approximate solutions of the equations of motion governing the phenomenon of interest.

In this section, we will discuss methods on the basis of porosity $\bar{\phi}$, correlation functions $S_n(\vec{r})$, $C_n(\vec{r})$, local porosity distributions $\mu(\phi)$. Table 2.1 shows the advantages and disadvantages of the geometric characteristics that are going to be used in this thesis.

Characterization	well defined	predictive	economical	easily usable
$\bar{\phi}, \dots$	yes	yes	yes	yes
$S_2\left(\vec{r}\right)$	yes	yes	yes	yes
$S_n\left(\vec{r}\right), \dots \left(n \geq 3\right)$	yes	yes	no	yes
$\mu\left(\phi\right)$	yes	yes	yes	yes

Table 2.1.: From [24, P. 318]. Advantages and disadvantages of different geometrical characteristics of porous media. We call a geometrical characterization economical if it requires the specification of less than 10^{12} numbers. $\bar{\phi}$ stands for porosity and other numbers (Minkowski functionals) that are going to be discussed later. $S_n\left(\vec{r}\right)$ is the correlation function between/among every n points. $\mu(\phi)$ is the local porosity distribution, that will be discussed later.

2.4.1. Porosity and specific internal surface

2.4.1.1. Porosity

Porosity is the most important characteristic of a porous medium. Most physical properties are influenced by it [24, P. 317].

For a two component or two-phases porous medium that consist of a pore space phase $\mathbb{P}$ (phase one) and a matrix phase $\mathbb{M}$ (phase two) where the whole sample $\mathbb{S}$ is defined as the union of those two phases $\mathbb{S} = \mathbb{P} \cap \mathbb{M}$ we define the porosity as the ratio

$$\phi\left(\mathbb{S}\right) = \frac{V\left(\mathbb{P}\right)}{V\left(\mathbb{S}\right)}, \tag{2.4.1}$$

which is basically the volume fraction of the pore space. $V\left(\mathbb{P}\right)$ denotes the volume of the pore space defined in Eq. 2.2.3, where we used the shorthand $V_3\left(\mathbb{P}\right) = V\left(\mathbb{P}\right)$, and $V\left(\mathbb{S}\right)$ is the total volume of the sample.

The definition 2.4.1 could be easily extended to stochastic porous media, by just having ϕ and $V\left(\mathbb{P}\right)$ as random variables. If the medium is homogeneous, one finds using 2.2.3 and 2.3.4

$$\begin{aligned}
\langle\phi\rangle &= \frac{V\left(\mathbb{P}\right)}{V\left(\mathbb{S}\right)} \\
&= \frac{1}{V\left(\mathbb{S}\right)} \left\langle \int_{\mathbb{S}} \chi_{\mathbb{P}}\left(\vec{r}\right) d\vec{r} \right\rangle \\
&= \frac{1}{V\left(\mathbb{S}\right)} \int_{\mathbb{S}} \left\langle \chi_{\mathbb{P}}\left(\vec{r}\right) \right\rangle d\vec{r} \\
&= \frac{1}{V\left(\mathbb{S}\right)} \int_{\mathbb{S}} \Pr\left\{r \in \mathbb{P}\right\} d\vec{r} \\
&= \Pr\left\{\vec{r}_0 \in \mathbb{P}\right\} \\
&= \left\langle \chi_{\mathbb{P}}\left(\vec{r}_0\right) \right\rangle,
\end{aligned} \tag{2.4.2}$$

where the last two statements hold only if the medium is stationary, and the $\vec{r}_0$ is an arbitrary point [24, P. 318]. As discussed formerly in Sec. 2.3.1, the expectation value used in the previous set of equations has to be applied on a discretized sample; nevertheless we used a continuous notation to indicate that it holds for the continuous case as well. If the stochastic medium is *mixing* or *ergodic* in addition to it being homogeneous and being infinitely extended, then the limit

$$\bar{\phi} = \lim_{R(\mathbb{S}) \to \infty} \phi\left(\mathbb{S}\right) = \langle\phi\rangle \tag{2.4.3}$$

exists and equals the porosity of the sample $\langle\phi\rangle$ [24, P. 319]. We define the diameter $R\left(\mathbb{G}\right)$ of a set $\mathbb{G}$ as $R\left(\mathbb{G}\right) = \sup\left\{|\vec{r}_1 - \vec{r}_2| : \vec{r}_1, \vec{r}_2 \in \mathbb{G}\right\}$ where $\sup$ is the supremum and indicates the supremum distance between pairs of points [24, P. 319]. $\bar{\phi} = \overline{\chi_{\mathbb{P}}\left(\vec{r}\right)}$ is a notation that indicates a spatial average while $\langle\phi\rangle = \langle\chi_{\mathbb{P}}\left(\vec{r}\right)\rangle$ is a configurational average.

Eq. 2.4.3 represents an ideal case [24, P. 319]. Geological porous media are often heterogeneous on all scales, for example see [2], which means that their volume fraction $\phi\left(R\left(\mathbb{S}\right)\right)$ would not reach a limit if $R\left(\mathbb{S}\right) \to \infty$. Eq. 2.4.3 assumes the homogeneity of the sample [24, P. 319] (Sec. 2.3). If such a sample is homogeneous the right length scale could be used to define what is called "representative elementary volume" [2, 1, 24].

2.4.1.2. Specific Internal Surface Area

The specific internal surface is an important characteristic of a porous medium just like the porosity. Actually, with a large surface to volume ratio a porous medium is loosely defined. The specific internal surface is an important measure for the surface to volume ratio [24, P. 320].

We define the specific internal surface for a two component porous medium as

$$S = \frac{V_2\left(\partial\mathbb{P}\right)}{V_3\left(\mathbb{S}\right)}, \tag{2.4.4}$$

where $V_2\left(\partial\mathbb{P}\right)$ is the surface area, as define in Eq. 2.2.3 of the boundary set $\partial\mathbb{P}$. In practical samples, the specific surface area exists as a finite value only if the internal surface ∂P fulfills suitable smoothness requirements. Fractal surfaces would have the value $V_2\left(\partial\mathbb{P}\right) = \infty$ [24, P. 320].

2.4.2. Correlation functions

Porosity and specific surface are merely two numbers that characterize the geometrical properties of a porous medium. It is obvious that these numbers are not sufficient at all for a detailed statistical characterization of the medium. A full characterization can be given by the multi-point correlation functions [24, P. 321].

The average porosity of the sample is given formerly in Eq. 2.4.2 as

$$\langle\phi\rangle = \langle\chi_{\mathbb{P}}\left(\vec{r}_0\right)\rangle = \Pr\left\{\vec{r}_0 \in \mathbb{P}\right\} \tag{2.4.5}$$

in terms of the expectation value of the random variable $\chi_{\mathbb{P}}(\vec{r}_0)$, where it takes the value 1 if the point $\vec{r}_0$ lies in pore space and otherwise 0 [24, P. 321]. This function is an example of a one-point correlation function. An example of a two-point point correlation function would be the *covariance function* $C_2(\vec{r}_0, \vec{r})$ which is the covariance of two random variables $\chi_{\mathbb{P}}(\vec{r})$ and $\chi_{\mathbb{P}}(\vec{r}_0)$ at two points $\vec{r}$ and $\vec{r}_0$,

$$C_2(\vec{r}_0, \vec{r}) = \langle [\chi_{\mathbb{P}}(\vec{r}_0) - \langle \chi_{\mathbb{P}}(\vec{r}_0) \rangle] [\chi_{\mathbb{P}}(\vec{r}) - \langle \chi_{\mathbb{P}}(\vec{r}) \rangle] \rangle . \tag{2.4.6}$$

For a homogeneous medium, the covariance depends only on the difference $\vec{r} - \vec{r}_0$, where setting $\vec{r}_0 = 0$ does not affect the generality of the measurement [24, P. 321]. This yields

$$C_2(\vec{r}) = \langle \chi_{\mathbb{P}}(0) \chi_{\mathbb{P}}(\vec{r}_0) \rangle - \langle \phi \rangle^2 .$$

Since $\chi_{\mathbb{P}}^2(\vec{r}_0) = \chi_{\mathbb{P}}(\vec{r}_0)$ it follows that $C_2(0) = \langle \phi \rangle (1 - \langle \phi \rangle)$. The correlation coefficient of two random variables X and Y is defined in general as ratio of the covariance $\text{cov}(X, Y)$ to the two standard deviations of X and Y [10, 11, 24]. The correlation coefficient varies between 1 and -1 corresponding to complete correlation or anti-correlation. The covariance function is normalized often to have a similar measure to the correlation coefficient by dividing it by $C_2(0)$ to obtain the two-point correlation function

$$G_2(\vec{r}) = \frac{C_2(\vec{r})}{C_2(0)} = \frac{C_2(\vec{r})}{\langle \phi \rangle \langle 1 - \phi \rangle} . \tag{2.4.7}$$

The general n-th moment function is defined [24, P. 322] as

$$S_n(\vec{r}_1, \ldots, \vec{r}_n) = \left\langle \prod_{i=1}^{n} (\chi_{\mathbb{P}}(\vec{r}_i)) \right\rangle , \tag{2.4.8}$$

where the average in the last equation is defined in Eq. 2.3.4 with respect to the probability density of the microstructure defined in Eq. 2.3.3.

2.4.3. Local geometry distribution

Local geometry distribution is one of the well defined geometric characterization of stochastic porous media [24, 14, 15, 16, 23, 25, 6]. We will discuss few types of geometry distributions that define different characteristics in a porous medium.

2.4.3.1. Local porosity distribution

Local porosity distribution can be defined for deterministic and for stochastic porous media [24, P. 332]. Consider partitioning a deterministic porous medium $\mathbb{S}$ to $\mathcal{K} = \{\mathbb{K}_1, \ldots, \mathbb{K}_M\}$, which are M mutually disjoint subsets, called *measurement cells* $\mathbb{K}_j$. Thus $\bigcup_{j=1}^{M} \mathbb{K}_j = \mathbb{S}$ and $\mathbb{K}_i \cap \mathbb{K}_j = \emptyset$ if $i \neq j$. A particular partitioning was used in the original publications [15, 16, 6, 20] where the $\mathbb{K}_j$ are unit cells centered at the vertices of a Bravias lattice superpositioned on $\mathbb{S}$. This offers the convenient feature that $\mathbb{K}_j$ are a translated set of itself. Fig. 2.4.1 represents the partitioning mentioned.
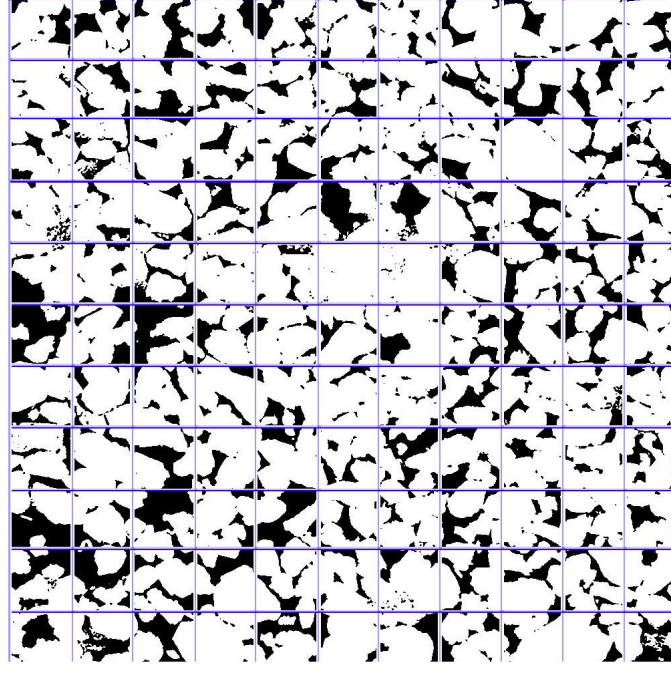
Figure 2.4.1.: Slice of a discretized and thresholded Bentheimer sandstone partitioned into a simple cubic lattice. Black color represents voids [24].

The local porosity in a measurement cell [24, P. 332] is

$$\phi(\mathbb{K}_j) = \frac{V(\mathbb{P} \cap \mathbb{K}_j)}{V(\mathbb{K}_j)} = \frac{1}{M_j} \sum_{\vec{r}_i \in \mathbb{K}_j} \chi_{\mathbb{P}}(\vec{r}_i), \tag{2.4.9}$$

where the second equality is there under the assumption of a discretized space, and M_j will denote total number of volume elements (or voxels) in $\mathbb{K}_j$. Thus the *empirical one cell local porosity density function* [24, P. 332] is defined as

$$\tilde{\mu}(\phi; \mathcal{K}) = \frac{1}{M} \sum_{j=1}^{M} \delta(\phi - \phi(\mathbb{K}_j)), \tag{2.4.10}$$

where $\delta(x)$ is the Dirac δ-function. Physically we define $\tilde{\mu}(\phi; \mathcal{K})$ as the probability for a cubic measurement cell within the side-length $\mathcal{K}$ to have the porosity ϕ [24, P. 332]. This distribution depends obviously on the cell size chosen for partitioning the sample space. Two extreme choices are to be discussed here and are of special interest [24, P. 332]. First one is setting $M = N$ (N is the total number of voxel in the discretized sample image), and thus, every $\mathbb{K}_j$ will contain one volume element $\mathbb{K}_j = \{\vec{r}_j\}$ with $1 \leq j \leq M = N$. In this case, every cell will have either the value $\phi(\mathbb{K}_j) = 1$ or $\phi(\mathbb{K}_j) = 0$ depending on whether the cell lies in pore space (1) or matrix (0). Thus the resulting distribution would be [24, P. 333]

$$\tilde{\mu}(\phi; \{\{\vec{r}_1\}, \ldots, \{\vec{r}_2\}\}) = \phi(\mathbb{S}) \delta(\phi - 1) + \phi(\mathbb{M}) \delta(\phi), \tag{2.4.11}$$

where $\phi(\mathbb{S})$ is the total porosity, and $\phi(\mathbb{M})$ is the total volume fraction of the other com-

ponents. The other extreme is for $M = 1$, and thus $\mathbb{K}_1 = \mathbb{S}$, meaning, that the only measurement cell contains the whole sample. In this case the distribution is, obviously,

$$\tilde{\mu}\left(\phi; \{\mathbb{S}\}\right) = \delta\left(\phi - \phi\left(\mathbb{S}\right)\right). \tag{2.4.12}$$

Note that both extremes determine the local porosity density through the total porosity $\phi\left(\mathbb{S}\right)$, where $\phi\left(\mathbb{S}\right) = \bar{\phi}$ if the sample is sufficiently large and ergodic, where 2.4.3 holds as well [24, P. 333].

For stochastic porous media, the extreme cases give similar results, after setting expectation values upon them. The first extreme gives the *one cell local porosity density function* [24, P. 333] defined for each measurement cell as

$$\mu\left(\phi; \mathbb{K}_j\right) = \left\langle \delta\left(\phi - \phi\left(\mathbb{K}_j\right)\right)\right\rangle, \tag{2.4.13}$$

where $\mathbb{K}_j \in \mathcal{K}$ is an element in the partitioned sample space. The other extreme, namely, when $M = N$, where $\mathbb{K}_j = \{\vec{r}_j\}$, one finds using Eq. 2.4.2

$$
\begin{aligned}
\mu\left(\phi; \{\vec{r}_i\}\right) &= \Pr\left\{X\left(\vec{r}_i\right) = 1\right\}\delta\left(\phi - 1\right) + \Pr\left\{X\left(\vec{r}_i\right) = 0\right\}\delta\left(\phi\right) \tag{2.4.14} \\
&= \left\langle\phi\right\rangle\delta\left(\phi - 1\right) + \left(1 - \left\langle\phi\right\rangle\right)\delta\left(\phi\right), \tag{2.4.15}
\end{aligned}
$$

which is independent of j [24, P. 334]. If mixing 2.4.3 holds then $\phi\left(\mathbb{S}\right) = \left\langle\phi\right\rangle = \bar{\phi}$ if the sample is sufficiently large, and the result becomes identical to Eq. 2.4.11 for deterministic media. One finds also in the other extreme of the coarsest partition [24, P. 334]

$$\mu\left(\mu; \mathbb{S}\right) = \left\langle\delta\left(\phi - \phi\left(\mathbb{S}\right)\right)\right\rangle, \tag{2.4.16}$$

which differs from 2.4.12 even if the sample is large, while mixing holds. This observation is important, because it emphasizes the necessity of considering more carefully the infinite volume limit $\mathbb{S} \to \mathbb{R}^d$.

2.4.3.2. Local percolation probability

In addition to the local porosity distribution it is necessary to characterize the geometrical connectivity of the porous medium. This is important for discussing transport properties which are highly sensitive to the connectivity of the medium, and less sensitive to its average porosity or specific internal surface [24, P. 340].

Two points inside the pore space $\mathbb{P}$ of a two-component porous medium are called *connected* if there is a path contained entirely within the pore space that connects those two points [24, P. 340]. With this connectivity criterion, a cubic measurement cell $\mathbb{K}$ is called percolating if there exists two points on the surfaces of the cell which are connected to each other [24, P. 340]. The *local percolation probability* $\lambda\left(\phi, S; \mathbb{K}\right)$ is defined [24, P. 340] as the probability of finding a percolating geometry in the measurement cells $\mathbb{K}$, whose local porosity is ϕ, and whose local specific internal surface is S. In practice, the estimator for $\lambda\left(\phi, S; \mathbb{K}\right)$ is the fraction of percolating cells which have the prescribed values of ϕ and S.

We define also the total *fraction of percolating cells* through the average local percolation probability

$$p\left(\mathbb{K}\right) = \int_0^\infty \int_0^1 \lambda\left(\phi, S; \mathbb{K}\right) \mu\left(\phi, S; \mathbb{K}\right) d\phi \, dS \qquad (2.4.17)$$

which is an important global geometric characteristic [24, P. 340].

2.5. Transport properties

The transport property, permeability, is investigated using a Lattice Boltzmann (LB) implementation and Darcy's law [34].

2.5.1. Permeability

The fluid's permeability, $\mathbf{k}$, in a porous medium is defined through Darcy's law

$$\left\langle v\left(\vec{x}\right)\right\rangle_{\vec{x} \in \mathbb{S}} = -\frac{1}{\eta} \mathbf{k} \left\langle \nabla p\right\rangle_{\vec{x} \in \mathbb{S}},$$

where $\left\langle \vec{v}\left(\vec{x}\right)\right\rangle_{\vec{x} \in \mathbb{S}}$ represents the fluid's average velocity in the whole sample, and $\left\langle \nabla p\right\rangle_{\vec{x} \in \mathbb{S}}$ is the average pressure gradient, and η is the dynamic viscosity of the fluid. The permeability, $\mathbf{k}$, is a second rank tensor [32]. The unit of permeability is m^2, but often the unit "Darcy" is used, $1\, D = 0.9869\, \mu\mathrm{m}^2$.

Darcy's law is derived from the homogenization of stationary Stokes equations for incompressible fluids

$$\begin{aligned}
-\nabla p\left(\vec{x}\right) + \eta \Delta \vec{v}\left(\vec{x}\right) &= 0, \\
\nabla \vec{v} &= 0,
\end{aligned}$$

with the boundary condition

$$\vec{v}\left(\vec{x}\right) = 0, \qquad \vec{x} \in \partial\mathbb{P},$$

where $\partial\mathbb{P}$ is the surface between the pores and matrix. The derivation can be found in [24] and the references there in.

3. Experimental sample

The following had been provided to us to study a Bentheimer sample

- μ-CT images for the Bentheimer

- grain size distribution for the modeling procedure.

In this chapter, we will discuss the analysis of the μ-CT images. The discussion and use of the grain size distribution will be postponed to Chapter 5.

3.1. Reading the data and visualizing it in 3D

The sample was provided in 831 files; every file represents a 2D slice of the 3D μ-CT dataset. The resolution of the images is $3.7\,\mu\mathrm{m}$. The files are binary images stored as 32-bit little endian byte order, float format with IEEE 754 standard. Every 2D image's slice size is 2048×2048 pixels; i.e., every pixel uses 4 bytes that represent a real number that in role represents a gray-scale value pixel. Fig. 3.1.1 shows a slice of the data provided.
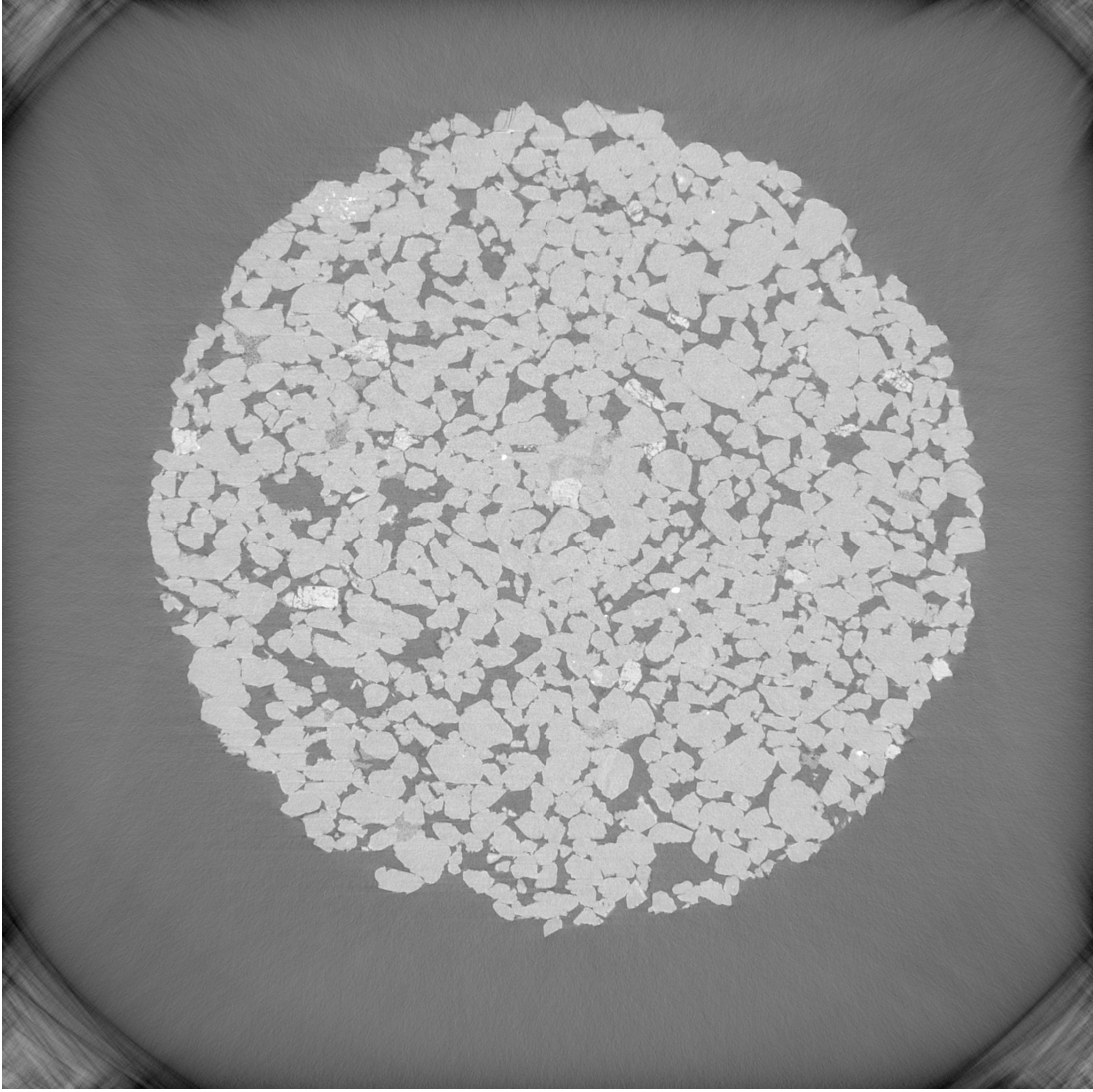
Figure 3.1.1.: 2D slice of a μ-CT image of Bentheimer sandstone at resolution $3.7\,\mu\mathrm{m}$. The brightness was enhanced for better visualization. The grains are shown in white, where as the pore-space appears in dark-gray.

In order to get rid of the useless regions, like ring artifacts (Fig. 3.1.2) and margins, the data was cropped from $2048 \times 2048 \times 831$ to $1024 \times 1024 \times 512$ voxels. Fig. 3.1.3 shows the same slice of Bentheimer in Fig. 3.1.1 after being cropped. The cropped images' boundaries are

$$
\begin{aligned}
x &\in [545, 1569]\,; \\
y &\in [466, 1490]\,; \\
z &\in [19, 530]\,,
\end{aligned}
\tag{3.1.1}
$$

where the first voxel is numbered 0 in every direction. Not unworthy to mention, that some ring artifacts are still there after the crop. The crop reduced them as much as possible, because they dominate in the last 200 2D slices of the dataset.
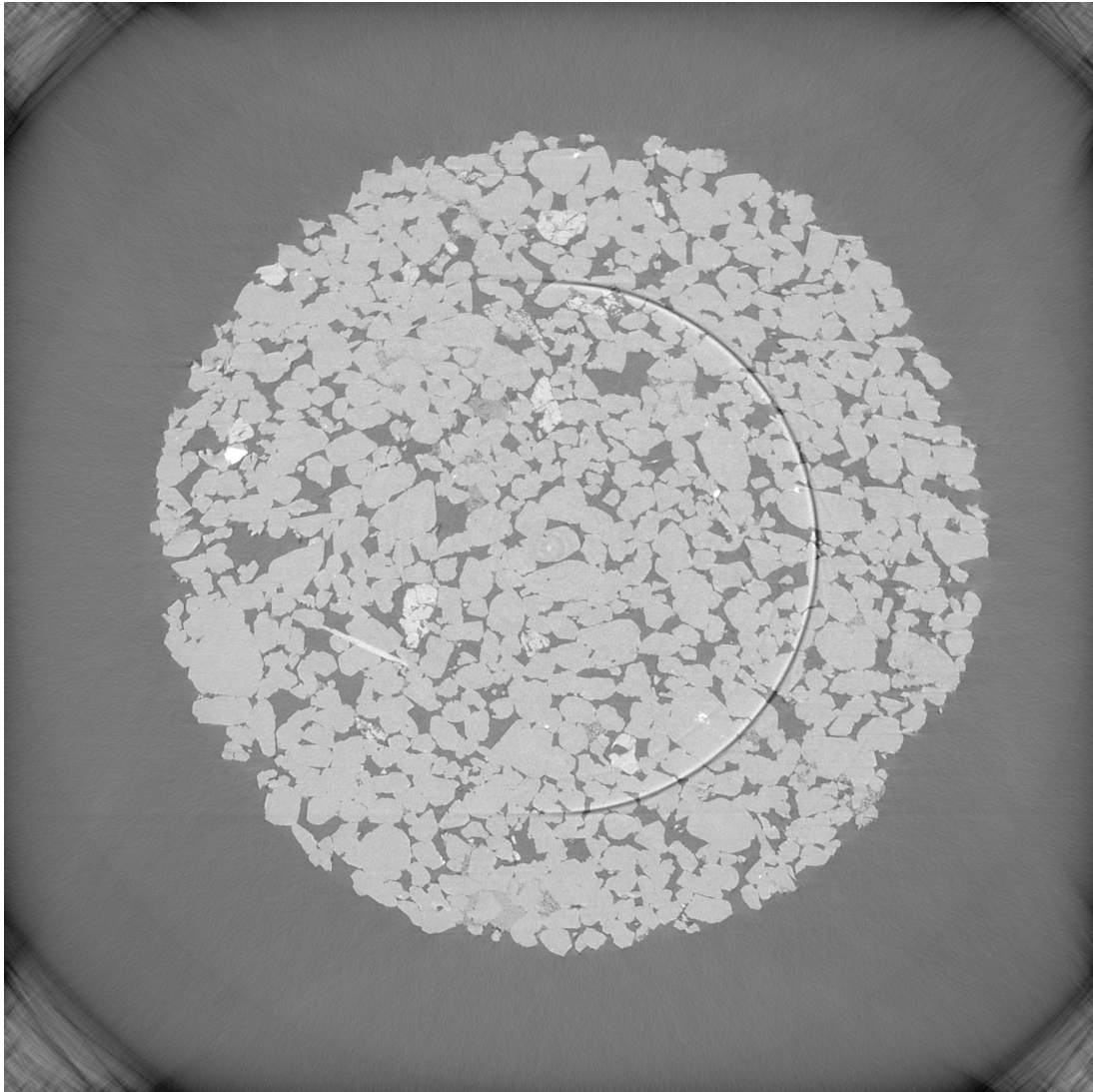

Figure 3.1.2.: Slice of the μ-CT data provided for Bentheimer. A ring artifact can be seen in this image.
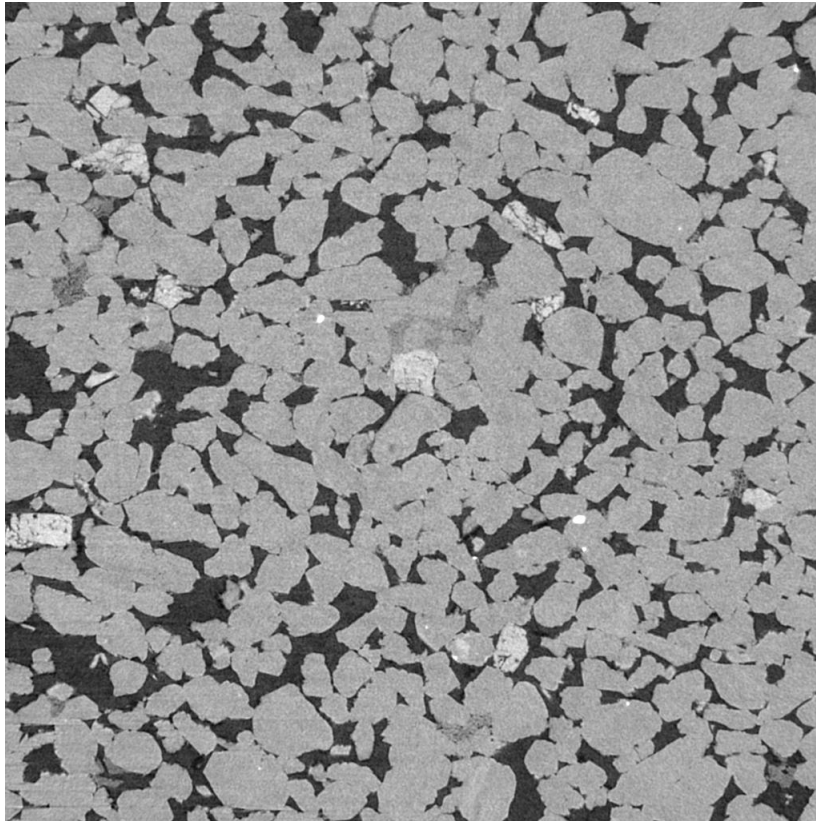
Figure 3.1.3.: Bentheimer μ-CT slice of Fig. 3.1.1 after being cropped by the dimensions given in Eq. 3.1.1.

3.2. Sample analysis

In the image shown in Fig. 3.1.3, three different phases (components) other than voids can be seen. We call them

- Normal grains

- Fillings

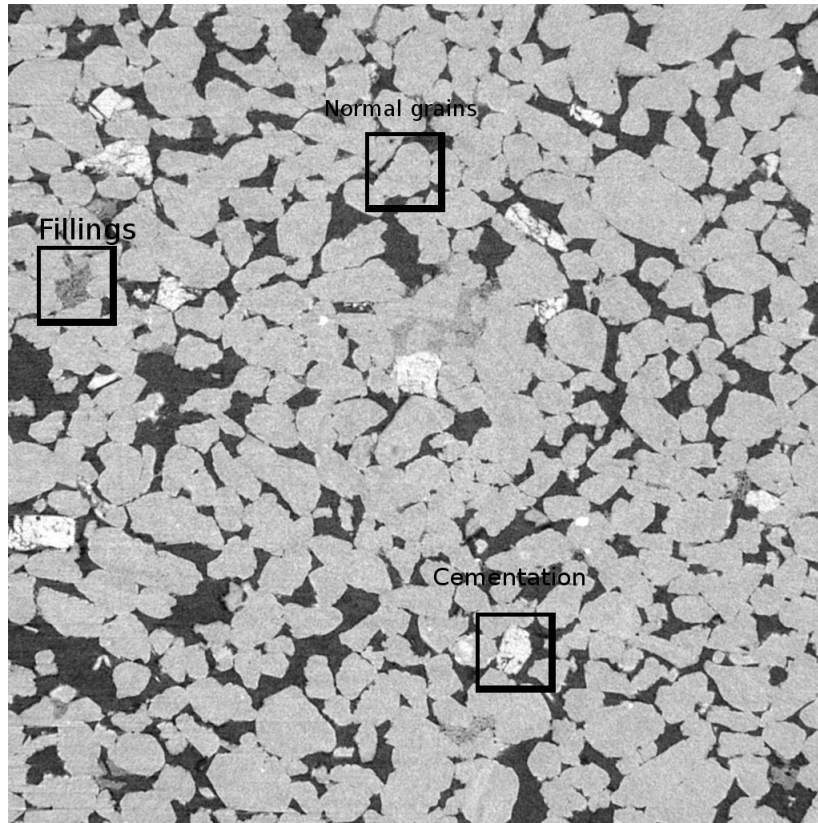- Cementations.

as shown in Fig. 3.2.1.

Figure 3.2.1.: Phases of Bentheimer sandstone.

3.2.1. Finding volume fractions of the phases

The first step in the analysis of the sample is finding the volume fraction of each phase. This step is done in order to determine the necessity of modeling each phase, and in order to find the appropriate G-function (primordial filter function) [5] for the sample if it is required. We start with statistics on the gray-scale values of the Bentheimer images. Fig. 3.2.2 shows a histogram for the gray-scale values of the experimental μ-CT images provided. We can see obvious two peaks. The high peak represents the gray-scale values of the normal grains, while the lower one represents the voids. This is confirmed by thresholding [12] the image and checking the effect of thresholding on the phases.
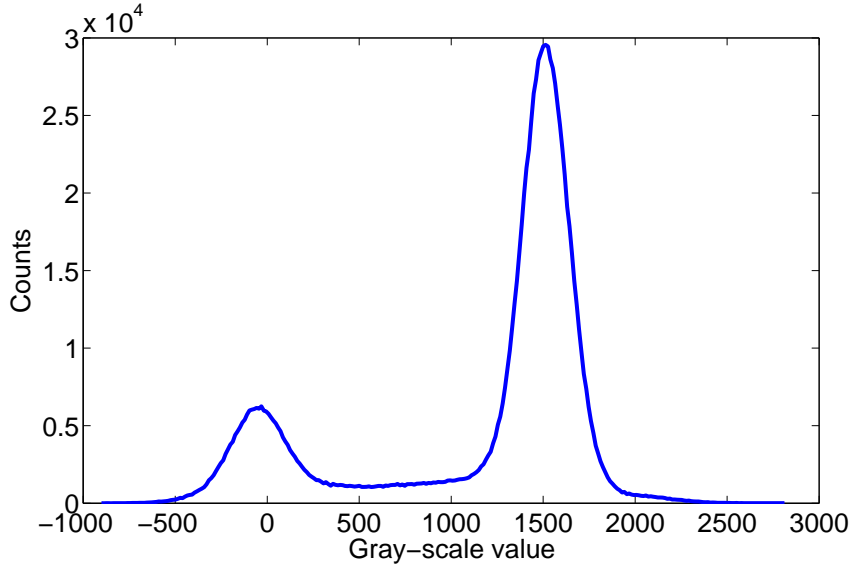
Figure 3.2.2.: Gray-scale values histogram for Bentheimer. We can figuratively see the phases mentioned in Sec. 3.2.1. The high peak represents the Normal grains, where we find them dominant. The short peak represents the voids, which are significantly present. The valley between the two peaks contains the fillings. The cementations are on the right to the high peak. Those observations were confirmed by thresholding the image and noticing the effect of different thresholds on the image.

It is important to make it clear, the difference between segmentation and thresholding. Thresholding is the mere operation of specifying a gray-scale value threshold that defines a characteristic function (Sec. 2.2). Meaning, for each pixel, if the gray-scale value is less than the threshold, it is assigned the value 0; otherwise, it is assigned the value 1. Segmentation is more complicated, where we are meant to separate every phase (or, in general, objects from an image) using any image processing means necessary.

Segmenting normal grains was not a problem due to their high volume fraction. The problem showed up with fillings where we see in Fig. 3.2.2 that the right threshold cannot be determined directly due to the low volume fraction of fillings, that is relatively low. Fig. 3.2.3 shows the result of trying to segment the fillings using bare thresholding. We can see that the rims of the normal grains are included in the threshold. This problem is due to the spatial color gradient between normal grains and voids; a part of it lies in the fillings' gray-scale region; i.e., in the valley in Fig. 3.2.2.

A similar problem was found for cementations. We can see in Fig. 3.2.3 that the spatial local fluctuations of normal grains' gray-scale values for every individual grain make the gray-scale values of cementations coincide with some regions in the normal grains; meaning, that the high peak in Fig. 3.2.2 contains some of the cementations regions. We can see, also, in Fig. 3.1.3 that cementations do not have a single color along their spatial region; the fact that causes them to appear "cracked" after thresholding as can be seen in Fig. 3.2.3.
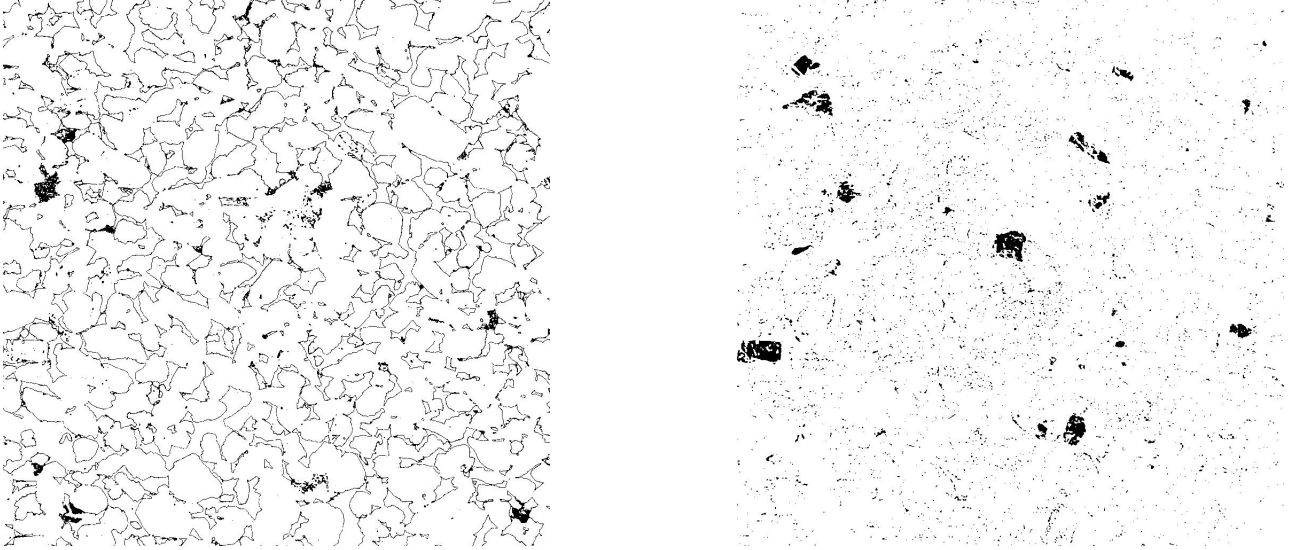
Figure 3.2.3.: Thresholding Bentheimer data. Slice of Fig. 3.1.3 is shown. Black color represents the desired regions. Left: thresholding fillings. The rims of normal grains are included in thresholding process. Right: thresholding cementations. Spurts from normal grains are included in the thresholded image due to the fluctuations of the spatial local gray-scale values of normal grains.

In the following we address this problem. A possible solution we proposed to the problem consists of three steps. First step is applying a median filter [12] to the data given, in order to make the gray-scale values locally homogeneous. The second step is, then, thresholding the gray scale image we get after applying the median filter. Then, finally, apply the Hoshen-Kopelman algorithm [26] (Appendix A.1) on the data that is converted to a binary image by thresholding (to the images' set that contains only ones and zeros). This process drops the rims seen in Fig. 3.2.3, since they do not form big clusters as we discuss in detail in Appendix A.1.

The median filter was applied in 3 pixels' depth as a compromise between achieving the purpose of the filter and not totally smearing the image. Fig. 3.2.4 shows the data from Fig. 3.1.3 after applying a 3-pixels depth median filter to it; however, the median filter does not suffice for getting rid of the rims that are found in Fig. 3.2.3.

The Hoshen-Kopelman algorithm was applied in order to retain the fillings; however, the standard algorithm was modified to achieve the desired purpose. Appendix A.1 explains the Hoshen-Kopelman algorithm in detail; it explains what we have altered in the algorithm to fit our purpose.
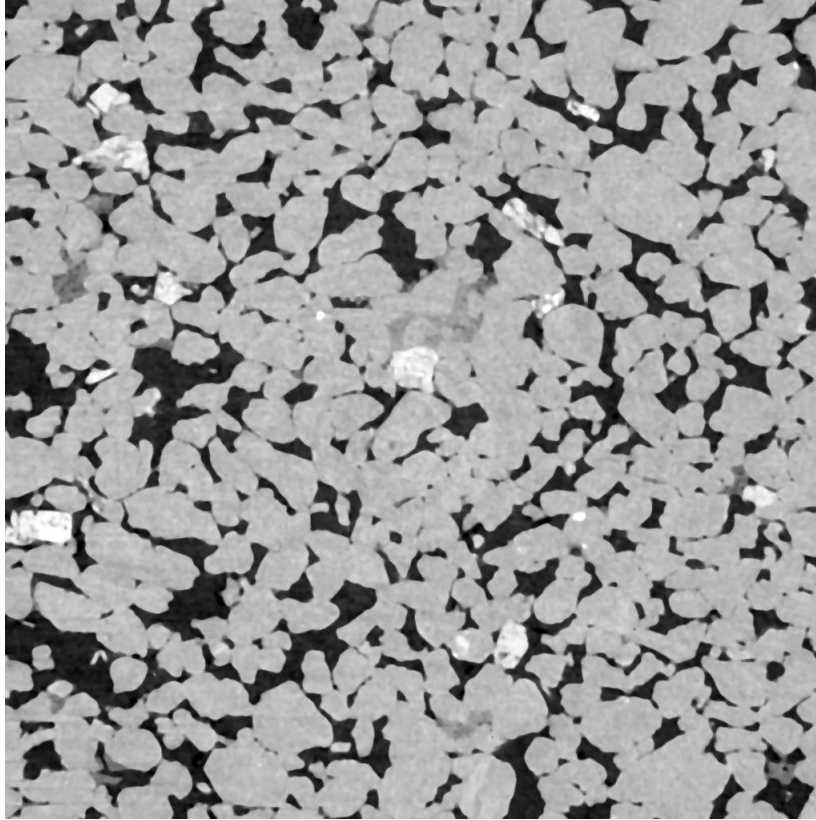
Figure 3.2.4.: Bentheimer μ-CT image slice from Fig. 3.1.3 after applying a 3-pixel depth median filter.

The image gray-scale thresholding was done, separately, for two subsequent ranges of gray-scale values; then, the Hoshen-Kopelman algorithm was applied on each binary image that resulted from each thresholding operation. This is done, because the rims, that we want to get rid off, are caused by a spatial gradient between normal grains and voids; this thresholding method makes the rims thinner; i.e., smaller clusters for better separation. Finally, the output of the two ranges were combined.

For the fillings, the cluster-size threshold (Appendix A.1) was chosen to be 1250 voxels. This threshold was chosen according to visual basis; it removes the rims found in Fig. 3.2.3 and retains the fillings. For the cementations, cluster-size threshold (Appendix A.1) was chosen to be 750 voxels on the same basis. Fig. 3.2.5 shows the output for the Hoshen-Kopelman algorithm for both fillings and cementations.
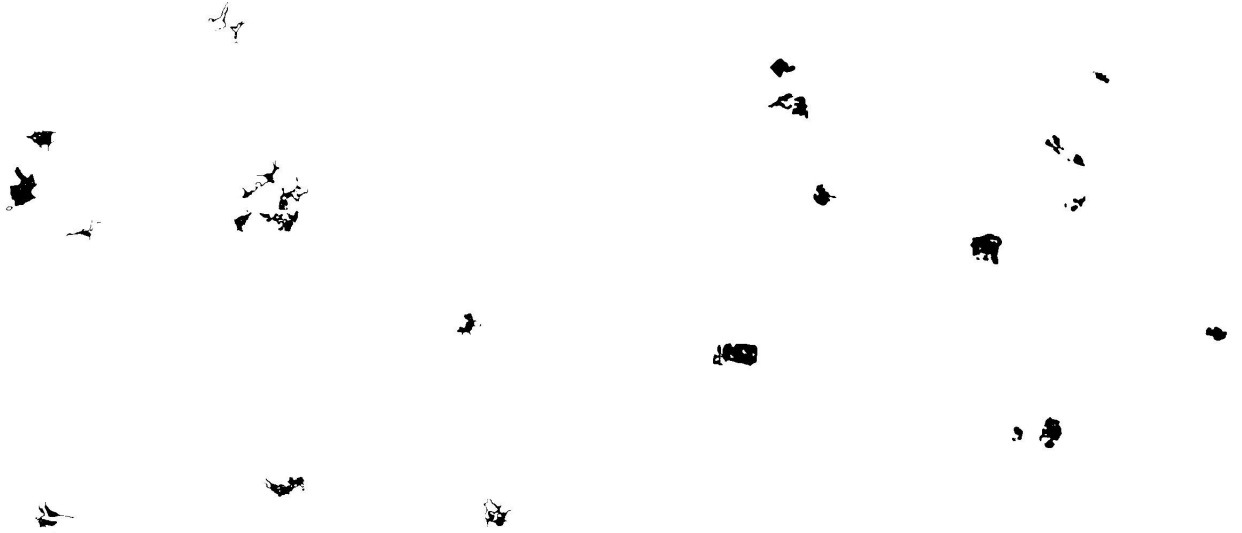
Figure 3.2.5.: The result of applying the Hoshen-Kopelman algorithm on Bentheimer sample. The original μ-CT slice is the one shown in Fig. 3.1.3. Black color represents the desired regions. Left: fillings. Right: cementations.

The volume fraction of fillings was found to be 0.93%, and for cementations 0.97%. In later sections, we show that those two phases are to be neglected due to their weak effect on the microstructure's characteristics, and due to the high efforts needed for their modeling.

Modeling cementations does not differ from modeling normal grains. We see from Fig. 3.1.3 that cementations have just a different color than normal grains, in addition to the cracks they have. Unfortunately, modeling them in their "cracked" form is not possible; however, we will consider them to be included in the standard modeling of the normal grains, i.e., nothing special will be done to model them.

3.2.2. Analyzing the segmented the sample

In this section, we try to find the best threshold that separates the normal grains from voids. We choose the threshold for the sample using Otsu's method [12, 36, 35]. Then, we threshold the sample at various gray-scale values around it.

Otsu's method Otsu's method [12, 36, 35], in computer science, is an algorithm for finding the optimum threshold to separate two classes of pixels; namely, foreground and background pixels (which is the case for voids and normal grains). The algorithm seeks a threshold that minimizes the within-class variance. The within-class variance is defined as the sum of variances of the two classes

$$\sigma_W^2 = \omega_1\left(t\right)\sigma_1^2\left(t\right) + \omega_2\left(t\right)\sigma_2^2\left(t\right), \tag{3.2.1}$$

ω_i are the probabilities of the two classes at a threshold t, and σ_i are the variances of these classes. Otsu showed that minimizing the within-class variance is equivalent to maximizing

the between-class variance

$$\sigma_B^2 = \omega_1\left(t\right)\left(\mu_1\left(t\right) - \mu_T\left(t\right)\right)^2 + \omega_2\left(t\right)\left(\mu_2\left(t\right) - \mu_T\left(t\right)\right)^2 = \omega_1\left(t\right)\omega_2\left(t\right)\left(\mu_1\left(t\right) - \mu_2\left(t\right)\right)^2,$$

with μ_T being the total mean at a threshold t

$$\mu_T\left(t\right) = \omega_1\left(t\right)\mu_1\left(t\right) + \omega_2\left(t\right)\mu_2\left(t\right)$$

where μ_i are the classes' means. The algorithm acts best on a gray-scale image that contains two peaks (as it is in Fig. 3.2.2). If there are more peaks, the algorithm, then, has to be modified for more classes; this operation is called "*Multithresholding*".

3.2.2.1. Minkowski functionals

The Minkowski functionals were measured using the algorithm in [30] for different thresholds; this is done in order to determine the error range for each characteristic. Table 3.1 shows the measurements of Minkowski functionals. This data is plotted in Fig. 3.2.6 for better understanding of the trend of Minkowski functionals as a function of the gray-scale threshold chosen for the Bentheimer experimental sample. Fig. 3.2.6 shows, also, an additional concern we had for the fillings. In each plot in Fig. 3.2.6 there are three curves; "Bare Threshold" represents the Minkowski functionals measured for the sample without altering it; i.e., from Table 3.1. "Fillings to matrix" shows the Minkowski functionals for the sample, while dealing with the fillings' regions that we segmented in Sec. 3.2.1 as if they were matrix. "Fillings to voids" shows the Minkowski for the sample, while dealing with fillings' regions as voids.

Threshold	300	500	700	766.98 (Otsu)
Porosity	0.17834	0.194381	0.209363	0.21468
Specific surface (mm^{-1})	15.7435	15.91	17.0047	17.3802
Mean curvature (mm^{-1})	114.656	318.307	316.346	298.743
Total curvature (mm^{-1})	49572.1	6259.52	-9878.03	-16154.4
Threshold	900	1100	Average	σ
Porosity	0.22587	0.245018	0.2113	0.0234
Specific surface (mm^{-1})	18.0627	19.1452	17.2077	1.2949
Mean curvature (mm^{-1})	249.684	248.967	257.7838	76.6801
Total curvature (mm^{-1})	-21554	9402.64	2941.3	25908

Table 3.1.: Minkowski functionals for different gray-scale thresholds of the Bentheimer sample. Thresholds are given in arbitrary units (Fig. 3.2.2). σ is the standard deviation.
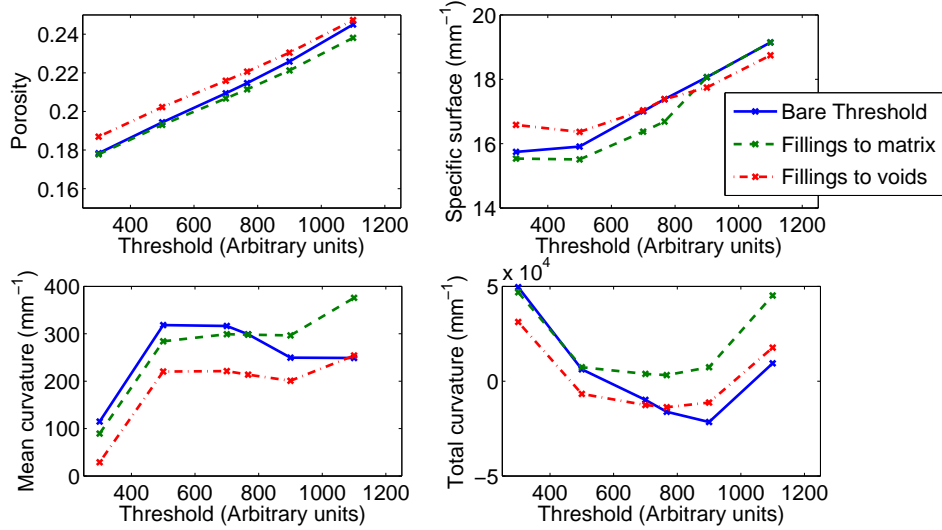
Figure 3.2.6.: Minkowski functionals as a function of the threshold in Bentheimer. The plots contain also the cases, where we consider the fillings regions once as matrix and once as voids.

The porosity curves, in Fig. 3.2.6, show that the gray-scale range we chose range from having fillings as voids to having them as matrix. The existence of fillings barely affect the porosity by 1%. The specific surface does not change greatly upon adding or removing matrix in fillings' regions. The mean and total curvature do not change monotonously; therefore, we cannot state any conclusion about them; however, the effect of fillings on them is negligible, compared with the standard deviation in Table 3.1.

We, now, have to decide, whether we have to model the fillings or not. From the previous discussion, we see that having or not having the fillings does not affect the microstructure's characteristics strongly, and does not pay back the computer efforts needed to model it. Modeling fillings is very expensive compared with what we need to model only one phase; therefore, we will drop this phase from modeling.

3.2.2.2. Two-point correlation function

The correlation functions was calculated for the thresholds mentioned in Table 3.1. Fig. 3.2.7 shows their correlation function. The plot shows that the correlation functions for those thresholds are almost identical.
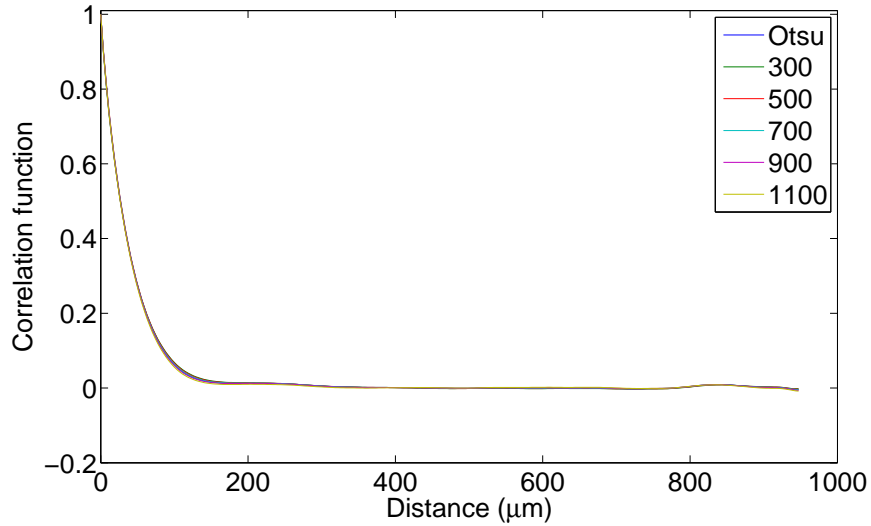
Figure 3.2.7.: Correlation function of the Bentheimer sample at different thresholds. We see that close threshold have almost identical correlation function. The lines drawn are thin; they are colored in order to make the comparison possible, since the curves are extremely close to each other.

3.2.2.3. Local geometry distribution

Local porosity measurements are costly and require, prohibitively, long time; the fact that has prevented us from doing the measurements for all thresholds. Here we present some of the measurements we have done. Most of the measurements were done for the sample thresholded by Otsu's method; this threshold is considered to be a compromise between the other thresholds.

Local porosity   Local porosity measurements, with different measurement cells' sizes, were done for the Bentheimer sample thresholded by Otsu's method. The cells' sizes vary from 32 voxels $(118.4\,\mu m)$ to 384 voxels $(1420.8\,\mu m)$. Fig. 3.2.8 shows these measurements.
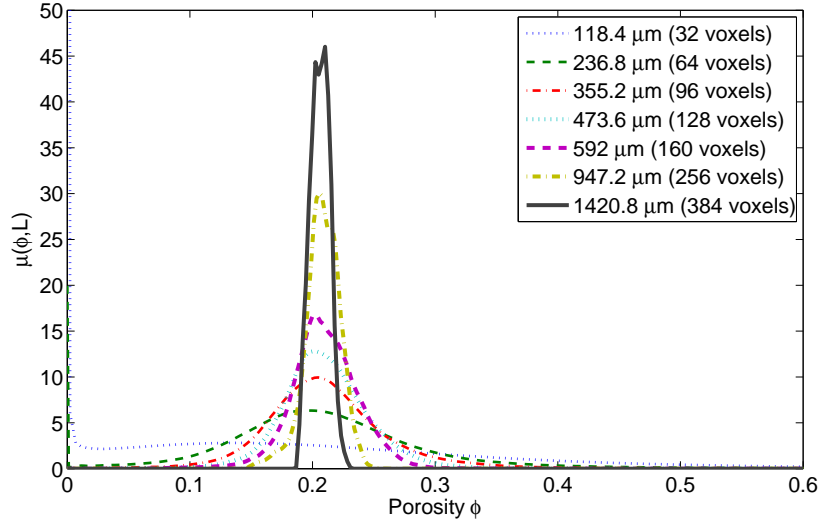
Figure 3.2.8.: Local porosity distribution for the Bentheimer's sample that is thresholded by Otsu's method with different measurement cell sizes. The measurement cell is always a cube. The legend specifies the side-length of the measurement cell for each curve.

As a compromise to get the other thresholds involved, Fig. 3.2.9 shows the local porosity distribution for the other thresholds, but with only one measurement cell size; namely, a cube with side-length 160 voxels $(592\,\mu\text{m})$. The systematic shift we find on them is due to the change in porosity that happens when varying the threshold [9].

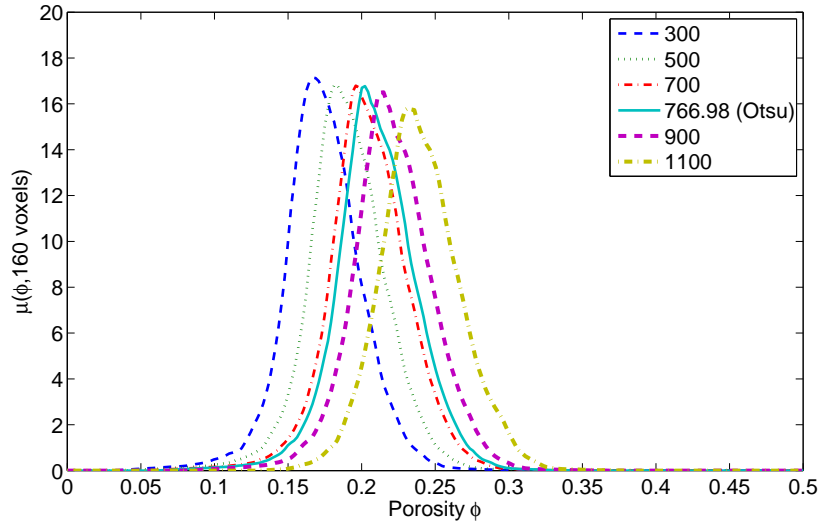Those results are to be compared later with the model we created.

Figure 3.2.9.: Local porosity measurements of the Bentheimer sample segmented with different thresholds, with a measurement cell size of 160 voxels $(592\,\mu\text{m})$.

Local percolation probability Local percolation probability distribution was only measured for Bentheimer sample thresholded by Otsu's method; the measurement is very costly. The sample was, also, cropped to the size $512 \times 512 \times 512$ voxels to make this measurement feasible. The measurement would last up to two months with the full size of the sample. With this crop the measurement time is reduced to one week. Fig. 3.2.10 shows the local percolation probability for the Bentheimer sample thresholded by Otsu's method. The measurements done in this thesis involve $\lambda_3 (\phi, S; \mathbb{K})$ (Sec. 2.4.3.2). This function gets the value 1 for each measurement cell if the cell percolates in three directions, and gets the value 0 otherwise. Those results are to be later compared with the model we created.

The local porosity distribution was measured for the same cropped sample, and the same measurement cell sizes, we used for the local percolation probability in order to calculate the total fraction of percolating cells.
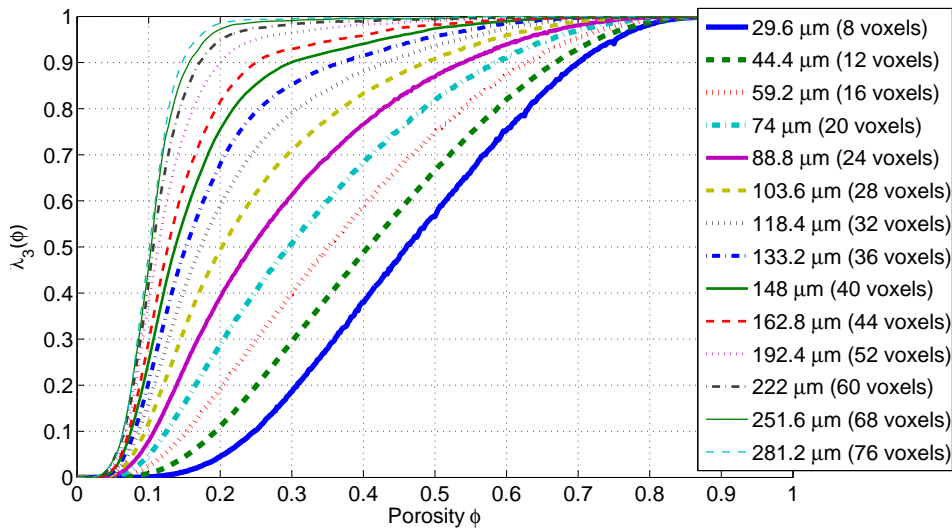
Figure 3.2.10.: Local percolation probability of the Bentheimer thresholded by Otsu's method with different measurement cell sizes. The measurement cell is a cube, the scales mentioned in the legend are the side-length of the measurement cube.

Total fraction of percolating cells Using the data of local percolation probabilities and local porosity distribution, we calculated the total fraction of percolating cells. Fig. 3.2.11 shows the total fraction of percolating cells for the Bentheimer sample thresholded by Otsu's method. This result will be later compared with the model we created. No further discussion will be stated for it in this section.
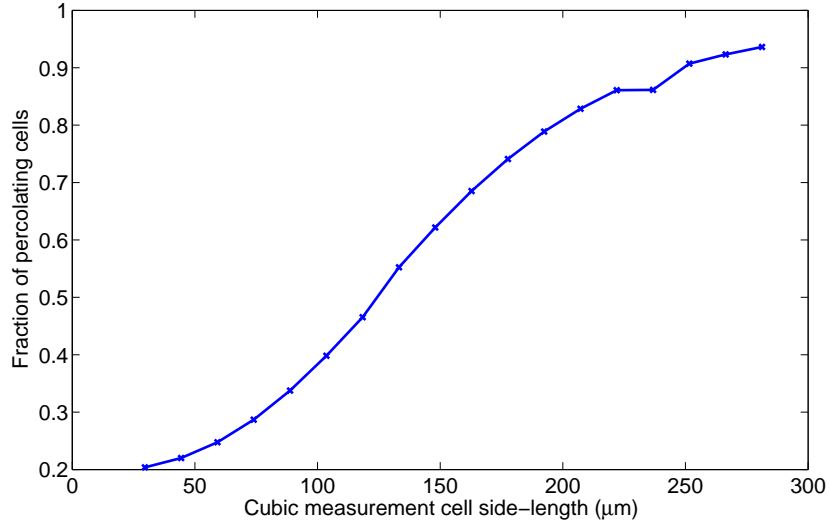
Figure 3.2.11.: Local fraction of percolating cells for the Bentheimer sample thresholded by Otsu's method.

3.2.2.4. Transport properties

A lattice Boltzmann flow implementation [34] was run on the sample after cropping it to the size $300 \times 300 \times 300$ voxels. The crop was done due to the extremely high memory the lattice Boltzmann simulation requires. Those results are to be, later, compared with the model we created.

Attribute	Value
Average velocity in z-direction	$1.35 \times 10^{-3}\,\mu\text{m}/\text{s}$
Variance of velocity in z-direction	$7.30 \times 10^{-6}\,\mu\text{m}/\text{s}$
Min-Max velocity in z-direction	$[-3.36 \times 10^{-2}, 1.81 \times 10^{-1}]\,\mu\text{m}/\text{s}$
Dynamic viscosity	$0.0264\,\text{kg}/\text{s}\cdot\mu\text{m}$
Global pressure gradient	$-4.31 \times 10^{-5}\,\text{kg}/\text{s}\cdot\mu\text{m}^2$
Permeability	$3.09\,D$

Table 3.2.: Lattice Boltzmann simulation results for Bentheimer sample thresholded by Otsu's method.

3.3. Conclusion and summary

In this chapter we dealt with a part of the provided data; namely, the μ-CT images of our Bentheimer sample. The analysis started by the concern of finding the volume fraction of each phase. This implied segmenting every phase into a binary image, or a characteristic function. Segmenting the normal grains was done by, simply, thresholding the μ-CT images.

This was possible due to this phase's high volume fraction. The other phases, cementations and fillings, were problematic due to their gray-scale values' interference with the normal grains, and due to their low volume fraction. The solution to the problem was accomplished using a modified Hoshen-Kopelman algorithm (Appendix A.1). Nothing special can be done for modeling cementations, since they differ from the normal grains by, only, their color and the cracks they have. The modeling technique we are using does not support such characteristics; therefore, modeling this phase will have no difference from modeling the normal grains; in other words, it will be dropped.

After segmenting the phases, we measured different characteristic of our Bentheimer sample. The first measurement was done for the Minkowski functionals. Through Minkowski functionals, and due to the low volume fraction of fillings, and judging from the high computer efforts needed for modeling this phase, we decided that we will ignore this phase totally. We measured also the two-point correlation function, local geometry distribution and, finally, a transport simulation was simulated on the sample. Through the transport simulation, we measured the permeability and other transport properties for the sample.

Now, after obtaining the measurements for our Bentheimer experimental sample, we turn into the methods and techniques we will be using to build the Bentheimer model.

4. Model generation

4.1. Introduction

The basics of the procedure we used to generate the Bentheimer model is described in [3, 31, 4], with some improvements. In this model, the rock occupying a bounded region $\mathbb{S} \subset \mathbb{R}^3$ is represented by crystallites placed in the continuum. Based on the depositional texture of the given rock, $\mathbb{S}$ is first divided into a number of different regions, each corresponding to distinct crystallite properties such as type, size, overlap, and orientation distribution. Crystallites for each of these regions are, separately, deposited in a random sequence, and then combined. Each element

$$\omega_i = (\vec{x}_i, R_i, \vec{a}_i, T_i) \tag{4.1.1}$$

of the sequence represents a crystallite of type T_i at spatial position $\vec{x}_i \in \mathbb{S}$ with inscribed sphere radius R_i and orientation $\vec{a}_i$.

In modeling of such rocks, the attributes of the crystallites defining the rock in the continuum need to be correlated with the primordial depositional texture of the rock. This is done by defining a gray-scale primordial filter function $G : \mathbb{S} \to [0, 1]$ that is carefully constructed from the images and geological information available on the rock. $G(\vec{x})$ is a given function that determines whether a crystallite can be deposited at $\vec{x}$ and of what size, orientation, type, etc. The crystallite attributes are defined through G as

$$R_i = \mathcal{R}\left(G\left(\vec{x}_i\right)\right); \tag{4.1.2}$$
$$\vec{a}_i = \mathcal{A}\left(G\left(\vec{x}_i\right)\right); \tag{4.1.3}$$
$$T_i = \mathcal{T}\left(G\left(\vec{x}_i\right)\right), \tag{4.1.4}$$

where $\mathcal{R} : [0,1] \to [R_{\min}, R_{\max}] \cup \{0\}$, $\mathcal{A} : [0,1] \to \mathbb{E}$, and $\mathcal{T} : [0,1] \to \{1, 2, \ldots, g\}$. $E = \{\vec{x} \in \mathbb{R}^3 : |\vec{x}| = 1\}$ is the unit sphere, $[R_{\min}, R_{\max}] \subset \mathbb{R}^1$ and g is the number of separate regions within the rock with distinct crystallite properties. If $\vec{x}_i$ falls in the pore space including the vuggy pores; $\mathcal{R}\left(G\left(\vec{x}_i\right)\right) = 0$, and no crystallite deposition is allowed there.

The procedure starts with packing spheres in a box; that we call *deposition*. Then, we assign grain shapes for those spheres and orient them; that we call *decoration*. Finally, we discretize this continuum model on a cubic grid; that we call *discretization*. In the following sections we discuss each step in detail.

4.2. Deposition

Packing spheres in a box has always been a challenging problem, especially when it comes to multiscale spheres packing, because the number of deposited spheres increase significantly for highly polydisperse packings.

   To ensure a fully supported matrix in the sphere packings, each deposited sphere has to have a finite overlap with at least one of the existing spheres. For two spheres labeled i and j having radii R_i and R_j, and having centers at positions $\vec{x}_i$ and $\vec{x}_j$. The overlap between these two spheres is defined as [3, 31, 4]

$$O_{i,j} = \frac{R_i + R_j - |\vec{x}_i - \vec{x}_j|}{R_i + R_j - |R_i - R_j|},$$
(4.2.1)

which has to be finite and smaller than $\lambda_i = \Lambda\left(G\left(\vec{x}_i\right)\right)$. This new function $\Lambda : [0,1] \to [\lambda_{\min}, \lambda_{\max}]$ also correlates the degree of spheres, i.e., crystallites, overlap with the primordial depositional texture through G.

   Many methods for spheres packing were implemented. In the following we discuss each one of them.

4.2.1. Monte-Carlo random deposition

This method is used in [31, 4]. In this method spheres are added sequentially by proposing in every step random coordinates and a random radius for each new sphere. Every newly added sphere has to have a finite overlap with at least one of the deposited spheres, otherwise the new sphere is rejected. The method in this simple concept is very costly and practically impossible to implement for a few reasons

- If we start with one initial sphere in the box to be filled, and then run the Monte-Carlo simulation. It is, then, almost impossible to have a finite overlap between the newly inserted sphere and the initial one in the box; the probability for the new sphere to hit the initial sphere is almost zero. Meaning, that we must have an initial sphere deposition pattern.

- If we assume that the deposition worked and the first problem is solved. While the deposition is evolving, and the box is filling up, the porosity will drop significantly, and the spheres in the box will become denser. Then, the struggle to find a free place to place a new sphere becomes harder and costly. Meaning, that reaching low porosity is almost impossible, which is very similar to the first problem.

- Checking the overlap for all the spheres, or for every two spheres, in the box is an n^2 problem along the deposition process. It becomes prohibitively costly, when the number of deposited spheres is high, or when there is a relatively high ratio of polydispersity.

A solution to these problems is dividing the box $\mathbb{S} \subset \mathbb{R}^3$ into smaller non-overlapping sub-cells (cubic cells), i.e., $\mathbb{S} = \mathbb{U}_1 \cup \mathbb{U}_2 \cup \mathbb{U}_3 \cup \cdots$. Not only this, but, also, ignore the lower overlap condition ($\lambda_{\min}$). In other words, depositing non-overlapping spheres, or with negative

overlap, is accepted; however, we rely on the high concentration of spheres to ensure their connectivity. The overlap is only checked for the spheres in the sub-cell being filled. The sub-cells for the deposition are filled randomly, not sequentially, in order to avoid correlations between the sub-cells.

This method causes the problem of making those sub-cells, $\mathbb{U}_i$, visible to the human eye when creating dense packings. This happens if we look to the packing's spheres as pattern points; i.e., representing every sphere as a point, and neglecting their radii. This problem happens due to the accumulation of the small spheres on the sides of the sub-cells; consequently, the deposition has lost its random attribute and homogeneity and obtained some correlations due to the improvements applied to the program.

4.2.2. Improved Monte-Carlo random deposition

The program that was already available for deposition had a lot of problems for me, personally, that I could not deal with. The person who has written the program, B. Biswal, and who had a role in [31, 4], had left the group, and the information available on the program was not sufficient to edit it and solve some memory leak and overflow problems and so on. Eventually, I decided to make my own program with the same basic scientific idea, based on the information I have in [31, 4]. After the creation of the program, I found that the idea could be enhanced, and the program could be improved. Unfortunately, the program was not investigated deeply due to the rise of the new deposition program using Molecular Dynamics (Sec. 4.2.3) created by T. Zauner and R. Hilfer, which exempted us, totally, from using the idea of Monte-Carlo deposition.

In the improved Monte-Carlo method, we divide the deposition process into two steps. The first step is similar to the normal Monte-Carlo deposition; we divide the region of deposition into non-intersecting sub-cells, and deposit spheres in each cell randomly up to a certain fraction of the total number of spheres that we want to deposit in each cell. The overlap is not only, then, checked for the sub-cell being filled, but also for a certain neighbors depth of sub-cells. For example, for neighbors depth of 1 cell, the overlap check will be done for each sub-cell of the 26 surrounding sub-cells (surrounding in three dimensions with depth of one, $3^3 - 1 = 26$), in addition to the sub-cell itself that is being filled, making the check total for $3^3 = 27$ sub-cells.

The next step is attaching spheres to the spheres deposited in the first step. This step is, first, done by proposing a random radius for the new sphere, R_j, using a uniform random number generator. Then, finding a random sphere among the ones already deposited and reading its radius, R_i, and its position, $\vec{x}_i$. Then we find the distance, that the new sphere has to have from the chosen sphere's center, that is already deposited, in order to fulfill the overlap condition, since the overlap is a function of the radii of the involved spheres, and the distance separating them. We do this as follows:

We solve Eq. 4.2.1 as an inequality of the maximum and minimum overlap for the distance as follows

$$\lambda_{\min} < \frac{R_i + R_j - |\vec{x}_i - \vec{x}_j|}{R_i + R_j - |R_i - R_j|} < \lambda_{\max}; \tag{4.2.2}$$

$$R_i + R_j - \lambda_{\min} \left(R_i + R_j - |R_i - R_j| \right) > |\vec{x}_i - \vec{x}_j| > R_i + R_j - \lambda_{\max} \left(R_i + R_j - |R_i - R_j| \right),$$
$$(4.2.3)$$

where $|\vec{x}_i - \vec{x}_j|$ is the distance between the spheres i and j. With this inequality, and having $\lambda_{\min}$ and $\lambda_{\max}$ pre-defined, we can calculate the distance range between the two spheres they need to have, so that they could have an overlap in the range $[\lambda_{\min}, \lambda_{\max}]$. Finally, proposing a distance in the right range us, using a uniform random number generator, will leave another two degrees of freedom unset; namely, the polar and azimuthal angles between the spheres. We set those angles by proposing random values for the components of the position vector, x_j, of the new sphere within the constraint

$$\sqrt{(x_i - x_j)^2 + (y_i - y_j)^2 + (z_i - z_j)^2} = |\vec{x}_i - \vec{x}_j|, \qquad (4.2.4)$$

where x_i, y_i, z_i are the components of the position vector, $\vec{x}_i$. With this information, we start attaching spheres to the ones already in the sub-cell. The attaching process includes an overlap check for each deposited sphere with the spheres in the current sub-cell and the neighboring cells (if there exist spheres in the neighboring sub-cells) within the specified depth, as we mentioned earlier in this section.

   This method, apparently, solved the problem of the cubic correlation we mentioned in the normal Monte-Carlo deposition, because the attached spheres do not necessarily lie in the same sub-cell; the new spheres are allowed to be deposited outside the current sub-cell. The advantages of the algorithm were not investigated deeply due to the rise of the new idea that will be discussed in the next section. The advantage I mentioned, i.e., the correlation problem, was confirmed only by viewing and comparing numerous different deposition patterns, that are created with both the old and new programs with the same input parameters.

4.2.3. Molecular dynamics

This method is a new idea, and has the advantage of speed over the previous two methods. In this method molecular dynamics was used; a repulsive potential if the spheres exceed the allowed limit of overlap and attractive if the particles are away from each other up to some limit. This is the method we chose for our modeling due to its high speed and efficiency in creating a homogeneous packings. The idea and program is currently under development in the group by T. Zauner and R. Hilfer. Details on the program should become clearer in publications later to come.

4.3. Decoration

The standard decoration procedure used in [4, 3, 31] implies assigning a polyhedron to every sphere and a random orientation for the Euler angles from a uniform random number distribution. The angles assigned are limited by a specified range, i.e., $[\theta_{\min}, \theta_{\max}]$. The polyhedra used formerly were almost isotropic, quartz crystallites and rombohedra in [31, 4]

respectively, in means of their diameter length and, thus, orienting them through a uniform random number generator was physically acceptable.

In Fig. 3.1.3, we see that a significant fraction of Bentheimer grains are elongated and anisotropic. In the following, a new elongated polyhedra creation method is devised. Also, a new method for orienting them to fit the needs of the Bentheimer sandstone is proposed.

4.3.1. Generating the polyhedra

Bentheimer sandstone, as can been seen in the μ-CT images provided (Fig. 3.1.3), has a variety of grain shapes in a way that makes it difficult to find a non-random way to model those grains with polyhedra. Here, an algorithm and methods we used in order to model Bentheimer grains on random bases are discussed.

The Bentheimer grains do not have a certain type or polyhedron figure that dominates, as the quartz crystallites in the case of Fontainebleau in [31], or the rombohedra in the sandstone in [4]; therefore, there was not a specific way to create polyhedra and call them the Bentheimer type. Problems arise, actually, with the fact that Bentheimer grains are anisotropic, thus elongated in many different ways (prolate, oblate and non-convex).

Therefore, some special procedure to create those polyhedra was used. A procedure that ensures totally stochastic outputs that look as much realistic as possible. Unfortunately, the techniques we used do not support the feature of non-convex polyhedra, so this feature will be dropped. This is due to the discretization algorithm that we will explain in Sec. 4.4.

The polyhedra created are a list of planes. A plane $\mathbb{A}$ is represented by a triplet (x, y, z). The way this plane is determined through these three components is the following. If we define a point $p = (x, y, z)$ in $\mathbb{R}^3$, then by definition $p \in \mathbb{A}$, and the plane is defined to be perpendicular to the vector $\vec{v}(x, y, z)$. In other words, we indicate to a plane by the corresponding vector $\vec{v}(x, y, z)$. This point guided us to randomly draw isotropic vectors that create a polyhedron, then, use them in the way we need them.

Therefore, the creation of our polyhedra is done in two steps

1. Placing planes on a unit sphere, i.e., creating n planes on a unit-sphere's surface by proposing random vectors perpendicular to its surface (method of inscribed sphere).

2. Elongating the created isotropic polyhedra in two directions by two random ratios (Method of polyhedron elongation).

4.3.1.1. Method of inscribed sphere

The planes are defined by vectors that point from the origin to a point on a unit sphere, where every plane is perpendicular to the vector's direction. This kind of definition is used since it is the form the discretization program accepts as input. The discretization program will be discussed in Sec. 4.4.

The task here lies in finding random vectors on a unit sphere. We use a pseudo-random point generator on the sphere's surface. This task is done by defining every vector as three scalar components x, y, z that have the magnitude 1. The method we use for those numbers is by the Cartesian-spherical coordinates conversion equations

$$
\begin{aligned}
x &= \sin\theta\cos\phi; \\
y &= \sin\theta\sin\phi; \\
z &= \cos\theta,
\end{aligned}
\qquad(4.3.1)
$$

where $\phi \in [0, 2\pi)$ and $\theta \in [0, \pi]$. The creation is done by setting M steps for θ and, then, L steps for ϕ. In every particular step for θ, we define θ_m values randomly where $0 \leqslant m < M$, and we define, also, in every step for θ_m the amount of L values for ϕ. Eventually, the planes' components will look as in Table 4.1 for every polyhedron.

x	y	z
$\sin\theta_0\cos\phi_0$	$\sin\theta_0\sin\phi_0$	$\cos\theta_0$
$\sin\theta_0\cos\phi_1$	$\sin\theta_0\sin\phi_1$	$\cos\theta_0$
$\sin\theta_0\cos\phi_2$	$\sin\theta_0\sin\phi_2$	$\cos\theta_0$
$\vdots$	$\vdots$	$\vdots$
$\sin\theta_0\cos\phi_{L-1}$	$\sin\theta_0\sin\phi_{L-1}$	$\cos\theta_0$
$\sin\theta_1\cos\phi_0$	$\sin\theta_1\sin\phi_0$	$\cos\theta_1$
$\sin\theta_1\cos\phi_1$	$\sin\theta_1\sin\phi_1$	$\cos\theta_1$
$\sin\theta_1\cos\phi_2$	$\sin\theta_1\sin\phi_2$	$\cos\theta_1$
$\vdots$	$\vdots$	$\vdots$
$\vdots$	$\vdots$	$\vdots$
$\sin\theta_{M-1}\cos\phi_0$	$\sin\theta_{M-1}\sin\phi_0$	$\cos\theta_{M-1}$
$\sin\theta_{M-1}\cos\phi_1$	$\sin\theta_{M-1}\sin\phi_1$	$\cos\theta_{M-1}$
$\sin\theta_{M-1}\cos\phi_2$	$\sin\theta_{M-1}\sin\phi_2$	$\cos\theta_{M-1}$
$\vdots$	$\vdots$	$\vdots$
$\sin\theta_{M-1}\cos\phi_{L-1}$	$\sin\theta_{M-1}\sin\phi_{L-1}$	$\cos\theta_{M-1}$

Table 4.1.: List of planes for every polyhedron in the first step of polyhedra creation. This set of planes have the problem that every L values in z are equal. This forms "rings" on the unit sphere's surface we are creating the points on; rings correspond to every value of z, which limits the quality of the planes being random. The solution is proposed in Table 4.2.

The resulting polyhedron will have $M \times L$ planes. The polyhedra are not written within this form in the output file. In order to avoid having "rings" of resulting vectors, i.e., single θ_m value for every L values of ϕ; another shuffling for every θ_m is done by adding or subtracting (choice is random) a random value to/from every θ_m. The value added is set in a way that it does not exceed θ_{m-1} by subtracting or θ_{m+1} by adding. The new polyhedron will look as in Table 4.2.

x	y	z
$\sin\left(\theta_0 \pm \xi_0\right)\cos\phi_0$	$\sin\theta_0 \sin\phi_0$	$\cos\theta_0$
$\sin\left(\theta_0 \pm \xi_1\right)\cos\phi_1$	$\sin\theta_0 \sin\phi_1$	$\cos\theta_0$
$\sin\left(\theta_0 \pm \xi_2\right)\cos\phi_2$	$\sin\theta_0 \sin\phi_2$	$\cos\theta_0$
$\vdots$	$\vdots$	$\vdots$
$\sin\left(\theta_0 \pm \xi_{L-1}\right)\cos\phi_{L-1}$	$\sin\left(\theta_0 \pm \xi_{L-1}\right)\sin\phi_{L-1}$	$\cos\left(\theta_0 \pm \xi_{L-1}\right)$
$\sin\left(\theta_1 \pm \xi_L\right)\cos\phi_0$	$\sin\left(\theta_1 \pm \xi_L\right)\sin\phi_0$	$\cos\left(\theta_1 \pm \xi_L\right)$
$\sin\left(\theta_1 \pm \xi_{L+1}\right)\cos\phi_1$	$\sin\left(\theta_1 \pm \xi_{L+1}\right)\sin\phi_1$	$\cos\left(\theta_1 \pm \xi_{L+1}\right)$
$\sin\left(\theta_1 \pm \xi_{L+2}\right)\cos\phi_2$	$\sin\left(\theta_1 \pm \xi_{L+2}\right)\sin\phi_2$	$\cos\left(\theta_1 \pm \xi_{L+2}\right)$
$\vdots$	$\vdots$	$\vdots$

Table 4.2.: The final output of the polyhedra's creation process. This table is a modified version of Table 4.1.

4.3.1.2. Method of polyhedron elongation

Elongating a polyhedron cannot be done trivially by, for example, multiplying the scalars x, y or z of Eq. 4.3.1 by an elongation ratio, because the planes are defined to be perpendicular to the vectors. This does not apply in the case of an ellipsoid which is the result of doing such an elongation operation. The result of such an operation would be losing the inner planes being swallowed by outer ones. Such planes would be included in the output, but will not be seen after discretizing the sample. In other words, they will only increase the computational efforts needed uselessly.

A method to elongate a polyhedron is shifting its planes in the direction of elongation. The shift is done by a value proportional to the cosine of the angle between the direction of elongation and the direction of the plane (its corresponding vector). For example, to elongate a polyhedron in z direction, we apply the following operation on every x, y and z

$$x' = x \cdot \frac{z}{\sqrt{x^2 + y^2 + z^2}} \cdot \eta; \tag{4.3.2}$$

$$y' = y \cdot \frac{z}{\sqrt{x^2 + y^2 + z^2}} \cdot \eta; \tag{4.3.3}$$

$$z' = z \cdot \frac{z}{\sqrt{x^2 + y^2 + z^2}} \cdot \eta, \tag{4.3.4}$$

where x', y' and z' are the planes after being shifted, η is the ratio of elongation.

This elongation is symmetric and does not affect the center of mass of the grain. Obviously, this elongation increases the volume of the grain in an uncontrollable manner when the elongation ratio is random. This makes it difficult to control porosity later (since the porosity will become a strong function of the polyhedra's orientation while the polyhedra are decorated with elongated polyhedra). This is the case, especially, if the deposition method used deposit spheres and not ellipsoids, which is the our case; where, obviously, the grains resulting from this algorithm are anisotropic.

4. *Model generation*

In the procedure for Bentheimer, this operation of elongation is done twice. Once for z direction and another for y direction. For every direction, a different and random η are chosen for each direction. This elongation procedure does not guarantee the polyhedron being oblate or prolate, because being elongated in one direction makes it prolate; and in two makes it oblate if the elongation ratios are equal, while this is controlled by random numbers (η in Eq. 4.3.2, 4.3.3 and 4.3.4).

In a try to retain the volume of the original elongated sphere, all planes are being shrunk by the ratio $\sqrt{\eta}$ isotropically. This is done by the operations in Eq. 4.3.5.

Note: the choice $\sqrt{\eta}$ was done as a compromise between leaving them elongated with much more volume than an isotropic object, and shrinking them by the ratio η which will make the polyhedra a lot smaller than the spheres that they are supposed to decorate.

$$
\begin{aligned}
x'' &= \frac{x'}{\sqrt{\max\left(\eta_y, \eta_z\right)}}; \\
y'' &= \frac{y'}{\sqrt{\max\left(\eta_y, \eta_z\right)}}; \\
z'' &= \frac{z'}{\sqrt{\max\left(\eta_y, \eta_z\right)}},
\end{aligned}
\tag{4.3.5}
$$

where η_y, η_z are the elongation ratios in the y and z respectively. x'', y'' and z'' are the elongated versions of x', y' and z' respectively.

In concept, those polyhedra are meant to decorate spheres on the deposition point pattern of the sample being created (by deposition, Sec. 4.2). The decoration shows that shrinking polyhedra this way makes them optimal within the volume of the sphere, and makes the polyhedron shorter than the meant sphere in a direction and longer in the other ones or vice-versa. Fig. 4.3.1[1] shows five random grains compared with the spheres they are supposed to decorate in the deposition pattern; the third shape on the right is the grain and the sphere combined in order to compare between their sizes. We see that the spheres always bump from one direction and get swallowed in the other two, or vice-versa.

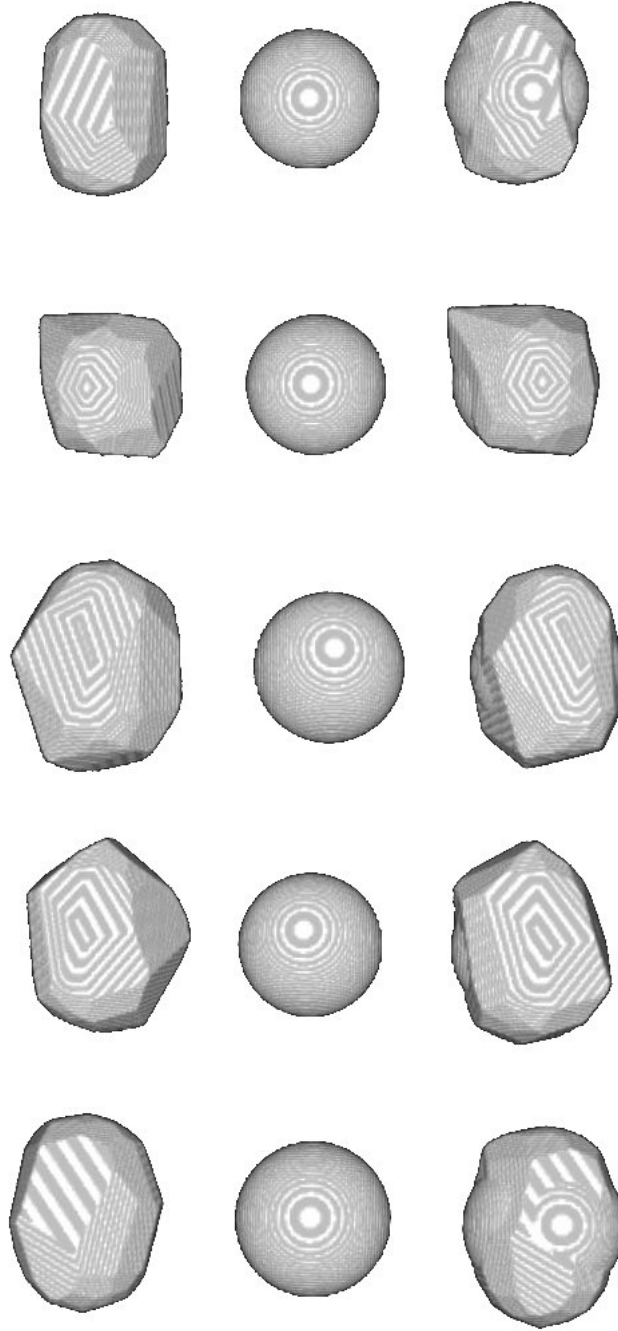[1]The polyhedra used in Fig. 4.3.1 are with 64 facets, and elongated by the ratio 0.7.

Figure 4.3.1.: Visualization of decorating spheres with polyhedra. The first column on the left shows the polyhedron that is an output of the polyhedra creation algorithm. The second column shows the sphere that is to be decorated by the polyhedron. The third column on the right shows the result of combining the polyhedron and the sphere together, in order to compare their volumes. We see that the spheres bump from the sides of the polyhedron, due to the shrinking we applied on them.

4.3.2. Overlap minimizer

The diagenesis process that creates sandstones causes the grains to have homogeneous overlaps in all directions regardless of the shape of the grain. This can be seen in Fig. 3.1.3. In Sec. 5.1.3, we will quantitatively prove that the overlap between Bentheimer grains is extremely low, and we will show the importance of lowering the overlap. The current deposition method, that is discussed in Sec. 4.2, has the problem that it takes into account only average radius for the calculation of the overlap; i.e., an isotropic sphere overlap.

4.3.2.1. Formulating the problem

After a deposition process, imagine two spheres with low overlap as Fig. 4.3.2 shows (and as we need in Bentheimer). If we randomly decorate those spheres with elongated polyhedra from Sec. 4.3.1, as it is done in [3, 31, 4], the spheres of Fig. 4.3.2 may, then, look as in Fig. 4.3.3.
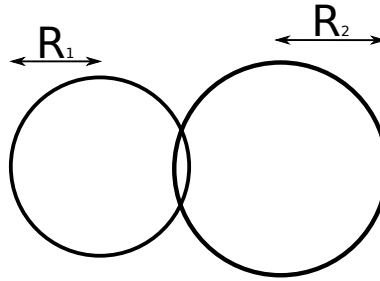

Figure 4.3.2.: 2D cross section of overlapping spheres as an outcome of the deposition process.
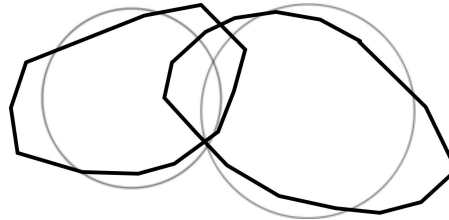

Figure 4.3.3.: Spheres from Fig.4.3.2 being decorated with grains in the decoration process.

In Fig. 4.3.3, we see that the overlap becomes greater; i.e., the polyhedra penetrate each other more than spheres did. This problem becomes more dominating when the elongation ratios of the polyhedra are greater, where the new overlap function between two polyhedra becomes dependent on the orientation of the decorating grains. Formerly, decoration, as mentioned in the introduction of Sec. 4.3, used to be done by a uniform random number generator; i.e., by assuming three random Euler angles. Such an approach would cause the formation of clusters of grains in the models (imagine the repetition of the case in Fig. 4.3.3), and an inhomogeneous distribution of voids, which is very unrealistic in a diagenesis processes

in nature. In this section we propose a method to lower the overlap by re-rotating the polyhedra and giving them a preferred direction through a Monte-Carlo simulation; i.e., by proposing new generalized quaternions that minimize the overlap.

4.3.2.2. Proposing a solution

The method we propose is finding what we call an *effective radius* rather than the standard sphere's radius we use, which depends on the orientation of the polyhedron.

Fitting polyhedra to ellipsoids   First, the polyhedra, that we obtained from the algorithm in Sec. 4.3.1, are fit to ellipsoids. This is done by finding the maximum values for the facets' components x, y and z for every polyhedron. Then, a new database containing the polyhedron number and its maximum x, y and z is created. The new database contains the equatorial radii $a = \max(x)$, $b = \max(y)$ and $c = \max(z)$ of the polyhedra. An ellipsoid fitting illustration is shown in Fig. 4.3.4.
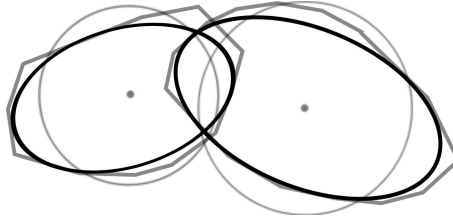

Figure 4.3.4.: Carrying on Fig. 4.3.2 and 4.3.3. Grains from Fig. 4.3.3 being fit by ellipsoids.

Finding nearest neighbors, or subdividing the sample   Then, the sample is analyzed. The problem lies in the fact that such a measurement, overlap measurement between every two spheres, is an n^2 problem; meaning, that it would take, prohibitively, long time to do the overlap measurement for big samples with high number of grains. Since we are concerned only about adjacent grains, and since finding adjacent neighbors is not a trivial matter, the solution we found for this problem is dividing the sample into sub-cells. Then, the overlaps in every cell and its neighboring cells within a certain integer depth N (neighboring cells depth) are measured.

What the program basically does, is going through every sub-cell, and picking every grain in that sub-cell. Then, for every grain in this sub-cell, it measures the overlap with the other grains within the same sub-cell and the grains within the neighboring sub-cells as well. This approach reduces the problem from an n^2 problem to a linear problem (n is the number of grains in the sample), if the length scale is chosen properly. Not to mention, that this approach becomes harder to apply for samples with high polydispersity.

Determining the effective overlap between every two ellipsoids   The new overlap is measured on the grounds of assuming two new spheres with effective radii that depend on the relative ellipsoids' orientations and on the line connecting their centers. If (x_1, y_1, z_1) is the center of the first deposited sphere, and (x_2, y_2, z_2) is the center of the second deposited

sphere. The *connection direction vector*, $\vec{v}$, is defined as the vector difference between the two center points, i.e.,

$$\vec{v}\,(v_x, v_y, v_z) = (\vec{x}_2 - \vec{x}_1)\,\vec{i} + (\vec{y}_2 - \vec{y}_1)\,\vec{j} + (\vec{z}_2 - \vec{z}_1)\,\vec{k}, \tag{4.3.6}$$

where $\vec{i}, \vec{j}, \vec{k}$ are the unit vectors on the axes x, y, z respectively. The line connecting those two ellipsoids' centers touches their surfaces at two points, those two points can be determined by the connection direction vector. Fig. 4.3.5 shows the line connecting the ellipsoids' centers and the points we need on their surfaces.
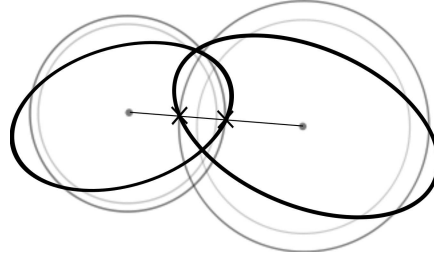

Figure 4.3.5.: The new radii of the spheres (the effective radii) that are set using the surfaces of the ellipsoids. The bright spheres are the ones done by deposition. The darker ones are the effective spheres. Notice that the effective spheres' radii are greater than the standard radii.
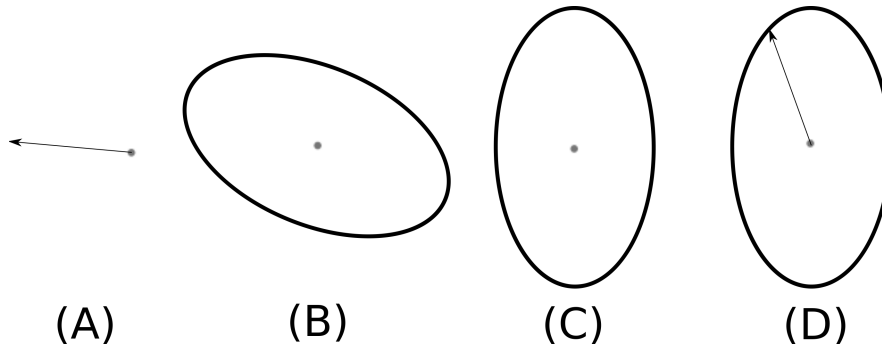

(A)   (B)   (C)   (D)

Figure 4.3.6.: The way we calculate the distance between the center and the point on the surface that is determined by the connection direction vector. The ellipsoid shown in this drawing is the one on the right in Fig. 4.3.5. A: is the connection direction vector from Fig. 4.3.5. B: is the ellipsoid from Fig. 4.3.5 copied with its orientation. C: is the ellipsoid without orientation, shown as it is stored in the database we created for the ellipsoids. D: shows that getting the distance between the center of the ellipsoid and the point on its surface, that is determined by the connection direction vector, could be done by inverse-rotating the connection vector, which, figuratively, rotates the ellipsoid to its original not-rotated situation.

To obtain the distance between the center of an ellipsoid and the point on the surface, that is being determined by the connection direction vector (the points in Fig. 4.3.5), we do an inverse rotation of the connection direction vector by the Euler angles for the meant grain (idea explained in Fig. 4.3.6). Since we have the equatorial radii of the ellipsoid, and the connection direction vector relative to the not-rotated ellipsoid, we can easily obtain the distance using the spherical coordinates equations and their conversion to Cartesian coordinates

$$
\begin{aligned}
x &= a \sin\theta \cos\phi; & (4.3.7) \\
y &= b \sin\theta \sin\phi; & (4.3.8) \\
z &= c \cos\theta, & (4.3.9)
\end{aligned}
$$

where θ and ϕ are obtained using the connection direction vector that we have applied the inverse rotation by the Euler angles upon. For that we use the equations

$$
\begin{aligned}
\theta &= \arccos\left(\frac{v_z}{\sqrt{v_x^2 + v_y^2 + v_z^2}}\right); & (4.3.10) \\
\phi &= \arctan\left(\frac{v_y}{v_x}\right), & (4.3.11)
\end{aligned}
$$

where $\arctan$, in Eq. 4.3.11, is the atan2 function, which is the inverse tangent function that distinguishes the diametrically opposite directions in an ellipsoid.

Substituting Eqs. 4.3.10 and 4.3.11 in Eqs. 4.3.7, 4.3.8 and 4.3.9; then, taking the magnitude of Eqs. 4.3.7, 4.3.8 and 4.3.9, gives the distance between the center of any ellipsoid and the points we need on the surfaces. With this, we obtain new radii for both ellipsoids, and then re-use the overlap formula

$$
O_{\text{eff}} = \frac{R_{\text{eff1}} + R_{\text{eff2}} - |\vec{x}_1 - \vec{x}_2|}{R_{\text{eff1}} + R_{\text{eff2}} - |R_{\text{eff1}} - R_{\text{eff2}}|},
$$

where $R_{\text{eff}i}$ are the effective radii of the ellipsoids in a certain orientation (the effective radii can be seen in Fig. 4.3.5 as the bigger gray spheres rather than the smaller ones). O_{eff} is the effective overlap between two ellipsoids.

Running the simulation Monte-Carlo simulation is then done to minimize this overlap. The program starts by measuring the effective overlap. If the overlap value is more than the allowed limit, it proposes new random Euler angles for the orientation, and re-measures the effective overlap. If the new proposed overlap is lower than the previously measured value, it is accepted. This process is iterated by a given number of tries for each grain; and the process is iterated, also, for every cell for a given number too.

4.3.2.3. Results of applying the overlap minimizer

The overlap minimization algorithm has succeeded in achieving its purpose, where applying it lowers the porosity of the sample significantly. Fig. 4.3.7 is a comparison between two decorations of the same deposition. The porosity of the one with random decoration is 0.273, where the one with the overlap minimizer has the porosity 0.218. The difference is, obviously, significant.
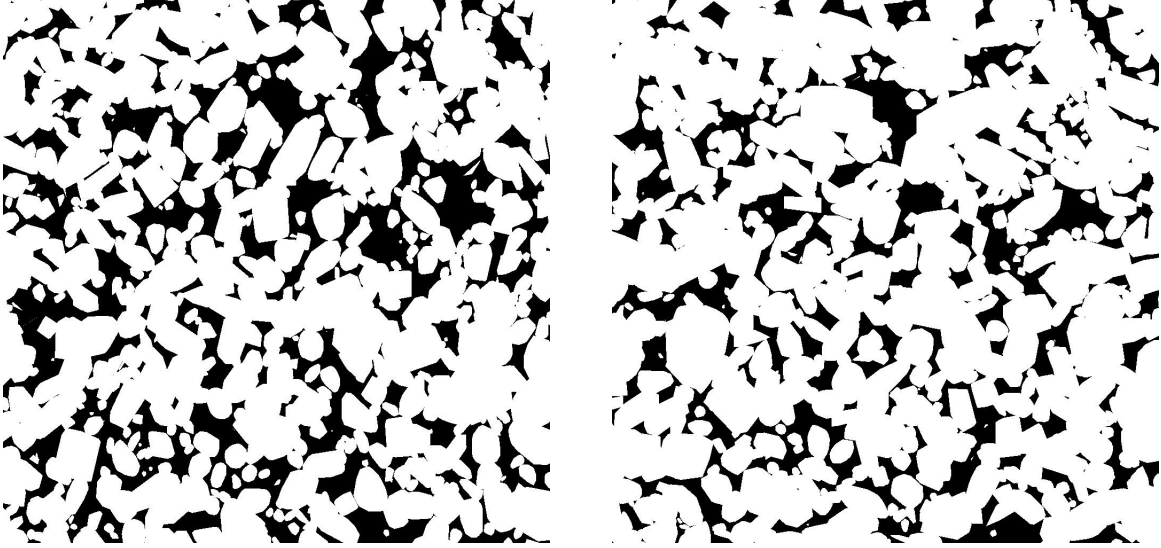

Figure 4.3.7.: A comparison between two slides of the same sample with random decoration (left) and decoration with overlap minimizing algorithm (right). We find that the sample with minimized overlap has a lower porosity; i.e., success in lowering the total overlap. In other words, less grains needed to achieve lower porosity, which makes more sense for Bentheimer as we can see in Fig. 3.1.3.

4.4. Discretization

After decoration, we obtain data-files containing the positions of the grains, radii (of the deposited spheres), their orientation Euler angles or quaternions and their crystallites (poly-hedra) types' identities of the polyhedra. This data has to be converted to a gray-scale image for measurements like porosity, specific internal surface and local geometry measurements to be accomplished.

The discretization algorithm is the one used in [31]. The discretization process is carried out by subdividing the cubic sample into a grid of cubic voxels, each of side-length $a\,\mu\mathrm{m}$. Inside each voxel a set of n^3 collocation points, i.e., an $n \times n \times n$ cubic sublattice, is placed symmetrically. The voxel is, then, assigned an integer m governed by the following rules:

- $m = n^3$ if all the n^3 collocation points fall inside the crystallites. This voxel represents matrix.

- $m = 0$ if all the n^3 collocation points fall outside the crystallites. This voxel represents pore space.

- $0 < m < n^3$ if m of the n^3 collocation points fall inside the crystallites. This voxel represents a combination of matrix and pore space.

The voxel label m, therefore, represents the density of the matrix volume in it. As a result, the gray-scale grid representation can be called a synthetic μ-CT image of the sandstone model at resolution $a\,\mu m$. Further, this image can be segmented by choosing a suitable threshold m_c. In such a binary representation, voxels with label $0 < m < m_c$ are relabeled to 0 (pore) and voxels with label $m_c \leq m \leq n^3$ are relabeled to 1 (matrix). The accuracy of the synthetic μ-CT can be increased by increasing n, the number of collocation points in each voxel.

The computational discretization procedure requires us to determine if a given collocation point falls inside any of the deposited crystallites, i.e., if a point p falls inside $\mathbb{G}_i$, $i = 1, 2, \ldots, N$, where $\mathbb{G}_i$ is the crystallite at position $\vec{x}_i$.

For each crystallite $\mathbb{G}_i$, $i = 1, 2, \ldots, N$, with the origin of the coordinate axes coinciding with x_i, the orientation $\vec{a}_i$ is defined by a sequence of three rotations of θ_1, θ_2 and θ_3 about the coordinate axes $\vec{e}_1$, $\vec{e}_2$ and $\vec{e}_3$ respectively, i.e.,

$$\vec{a}_i = \hat{\mathcal{Q}}_{i3} \hat{\mathcal{Q}}_{i2} \hat{\mathcal{Q}}_{i1} = \hat{q}_i.$$

The polyhedra we created in Sec. 4.3, as we mentioned, consist of K planes that form a closed object. The discretization procedure involves determining if a given point falls inside any of the crystallites. A specific point $\vec{p}$ falls inside the crystallite $\mathbb{G}_i$, $i = 1, 2, \ldots, N$ if

$$\vec{n}_j \cdot \left(\frac{1}{d_i} \vec{p}_i' - \vec{n}_j \right) < 0, \quad j = 1, \ldots, K,$$

where $\vec{n}_j$ are the normal vectors (explained in 4.3.1) that specify $\mathbb{G}_i$, $\vec{p}_r' = q_i^{-1} (\vec{p} - \vec{x}_i) \left(q_i^{-1} \right)^*$ and $(\cdot)^*$ is the quaternion conjugation.

Fig. 4.4.1 shows the idea of going from spheres in pack (from deposition, Sec. 4.2) and use the decoration data (data from Sec. 4.3) to get discretized polyhedra. We see that the deposition spheres are circumscribed by the polyhedra.
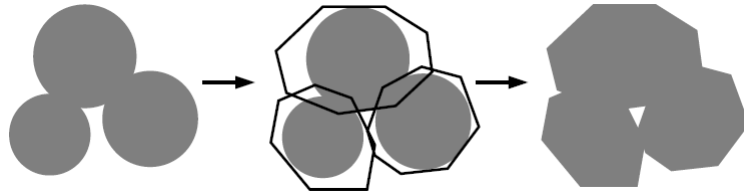

Figure 4.4.1.: Decorating spheres with polyhedra in the discretization process. Spheres are circumscribed by the polyhedra. Figure taken From [31].

4.5. Conclusion

In this chapter, we presented three different methods for packing multiscale spheres. The best method was the method of Molecular Dynamics, in terms of computational efforts. Then, we turned into generating the right polyhedra for decoration of Bentheimer. The polyhedra we created are generated randomly, and are characterized by the number of facets they have, and their maximum elongation ratio. The Bentheimer sample has elongated polyhedra; the issue that dragged a new problem into the field, as a consequence of using spheres deposition algorithm and then decorating them by elongated polyhedra. The problem is that the overlap of the grains is a function of their orientations, and as a consequence, the porosity could change with different orientations. This problem did not exist formerly, because the previous sample had almost isotropic polyhedra, in means of diameter lengths. For this problem, we had to create what we called an "overlap minimization algorithm". In this algorithm, a Monte-Carlo simulation is run in order to minimize the overlap of each grain by re-orienting it and re-measuring the overlap, which is an iterative process. Finally, we discussed how the discretization process is done, which is the same algorithm used in [31, 3].

In the next chapter, we study the tend of the microstructure's characteristics as functions of the model building parameters we learned in this chapter.

5. Achieving the Bentheimer model systematically

5.1. Parameter study

To determine the appropriate parameters for the reconstruction of the Bentheimer sample, the model parameters were systematically analyzed. Their influence on the Minkowski functionals and other microstructure's characteristics is investigated, and the resulting models are visually compared to the original sample on 2D cross sections.

In the comparison of measurements results, we concentrate on the Minkowski functionals (porosity, specific surface, mean curvature and total curvature), local porosity distribution and the two-point correlation function. Those choices were done according to the feasibility of doing the measurement, since measuring some quantities, like local percolation probability, is very costly and would take, prohibitively, long time.

Important note about the local porosity distribution

The number of measurements depend only on the size of the sample and on the measurement cell size; consequently, the area under the local porosity distribution's curve is, always, the same for the same measurement cell and the same sample size. This is caused by the algorithm used. In other words, we can reduce the curve's shape description, or means of comparison, down to two characteristics. First one is its sharpness (height of its peak), and the second is its shift (peak's value on the x axis). We are concerned only about the sharpness, because the shift depends totally on the average porosity of the sample, if the sample is homogeneous, which can controlled by other parameters easily (like the number of spheres to be deposited in the deposition process).

5.1.1. Grain size distribution rescaling

As it is mentioned in Chapter 3, we had been provided a *grain size distribution* for Bentheimer. The grain size distribution had to be rescaled in order to fit the polyhedra that we created, since the grain size distribution has to be used for spheres deposition (Sec. 4.2), where the polyhedra size is affected by the elongation process we mentioned formerly in Sec. 4.3.1.2. We considered that the grain size distribution provides diameters for the spheres in the deposition process; we, then, applied the rescale.

In the following we measured some geometrical characteristics for five models. In every model the grain size distribution is rescaled. The models created by rescaling size distributions

to 78%, 79%, 80%, 81% and 82%. Table 5.1 shows a comparison between Minkowski functionals of those models, compared with the thresholded experimental sample using Otsu's method (labeled "Otsu" in the table) (Sec. 3.2.2). Fig. 5.1.1 is a plot for the table's values.

Fig. 5.1.2 shows a comparison between the local porosity distribution of the models from Table 5.1 and the Bentheimer that is thresholded by Otsu's method (Sec. 3.2.2).

	Otsu	78% (7b)	79% (7e)	80% (7a)	81% (7d)	82% (7c)
Porosity	0.21	0.21	0.205	0.19	0.19	0.18
Specific surface	17.38	13.43	13.14	12.64	12.38	11.95
Mean curvature	298	101	107	122	123	132
Total curvature	-16154	-2415	-1936	-1607	-1369	-627

Table 5.1.: Comparison between five built models with different grain size distribution rescaling. Minkowski functionals of the models are compared with the Bentheimer sample thresholded with Otsu's method (Sec. 3.2.2).
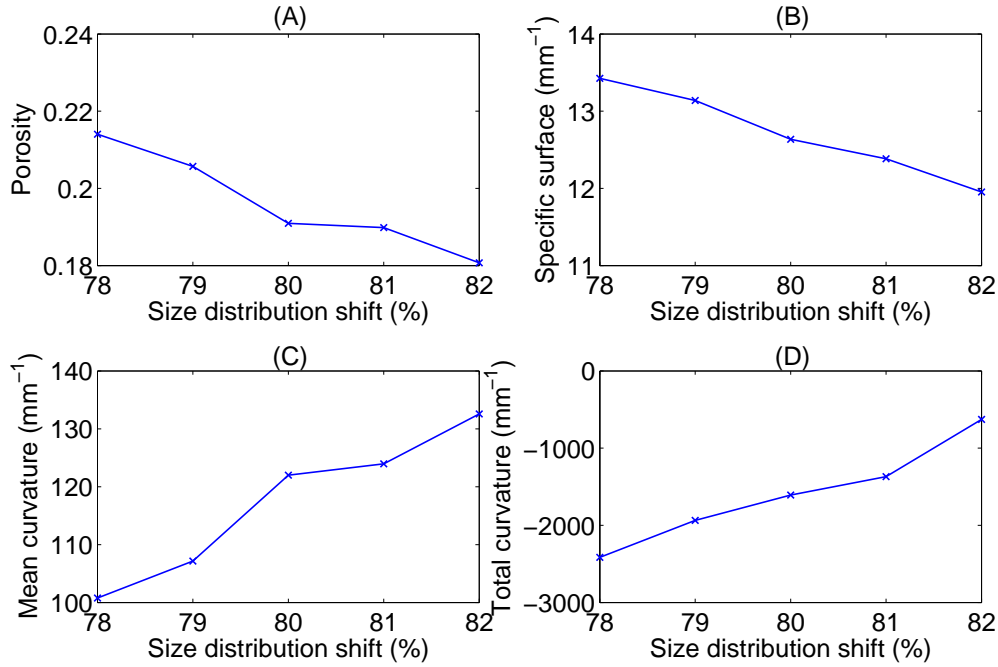

Figure 5.1.1.: The effect of rescaling the size distribution upon the Minkowski functionals. (A): effect on porosity. (B): effect on specific surface. (C): effect on mean curvature. (D): effect on total curvature.

As it is intuitively expected for the porosity, the increase of the grain sizes decreases the porosity noticeably. We see from Table 5.1 that different rescaling within the range 5% could give a porosity change up to 4% in a semi-linear manner. Which means that controlling the porosity through grain size distribution is not a difficult task and feasible. One has to be

careful while doing this tweaking, since rescaling the grain size distribution does not only affect the porosity, but also significantly the specific surface. The relative difference of the specific surface within the chosen range of rescaling is 11%, which means that specific surface is pretty sensitive to rescaling the grain sizes; therefore, one needs to study other parameters to do this tweaking right. Surprisingly, and not as expected for the mean curvature and total curvature from their characteristics found in Sec. 3.2.2 with different thresholds, they showed monotonic behavior that gave us the possibility to control them up to some point.
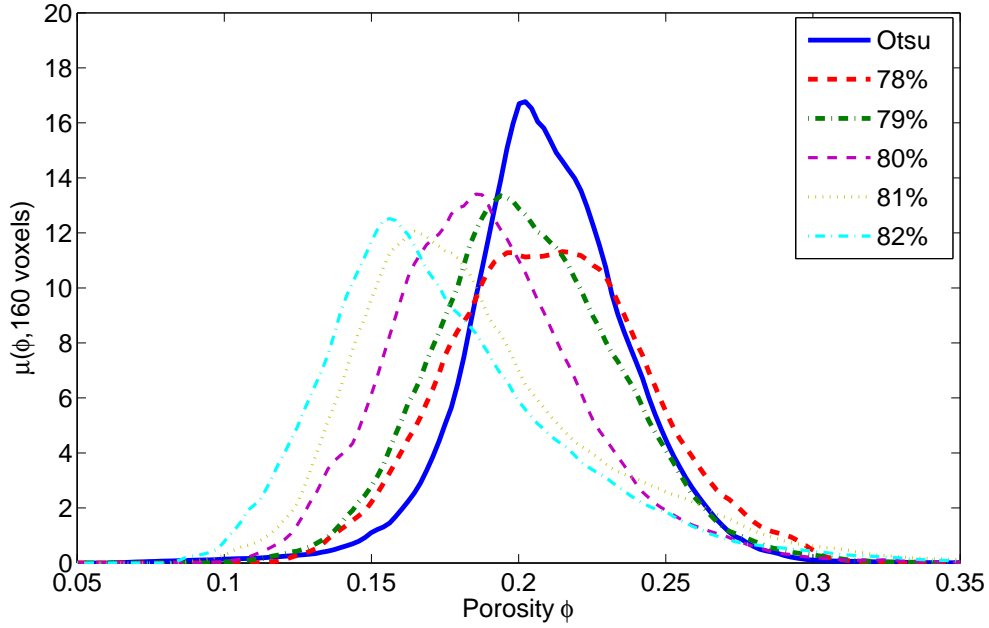

Figure 5.1.2.: Comparison of the local porosity distribution between the models of Table 5.1 with the Bentheimer sample thresholded by Otsu's method (Sec. 3.2.2). Measurement cell is a cube with side length 160 voxels. We see that rescaling the size distribution does not have a monotone profile in affecting the height of the curves, but only shifts them due to the change in porosity.

The local porosity distributions' shapes, as we can see from Fig. 5.1.2, did not change systematically in its sharpness, but only shifted systematically into the negative x direction due to the decrease in porosity (for the definition of sharpness, refer to the introduction of Sec. 5.1).
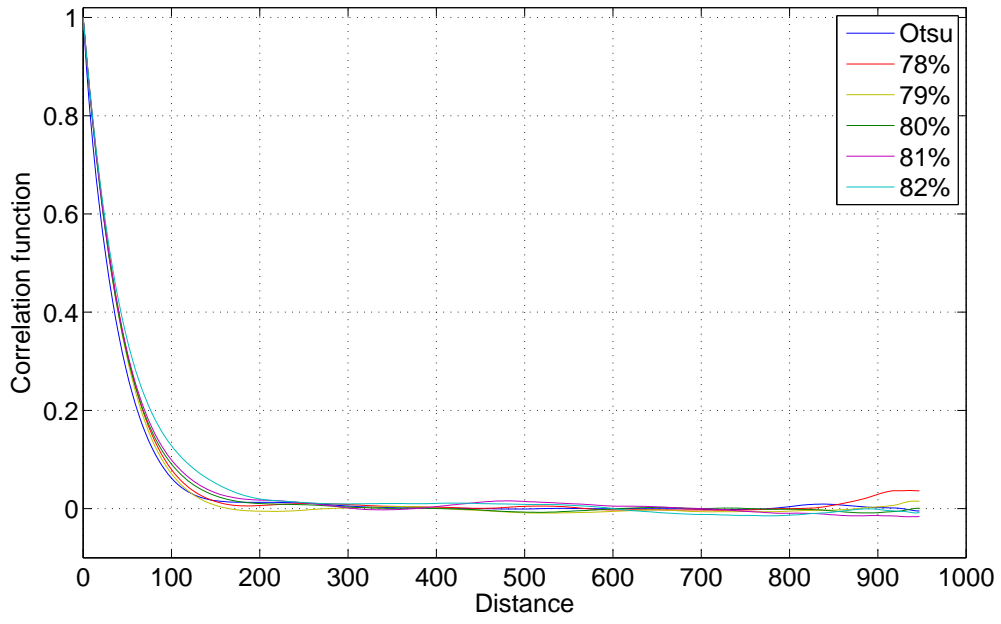
Figure 5.1.3.: Correlation function of Bentheimer model upon rescaling the sizes of the grains. Curves are colored and thin due to their closeness. For better understanding of the difference, please refer to Fig. 5.1.4.
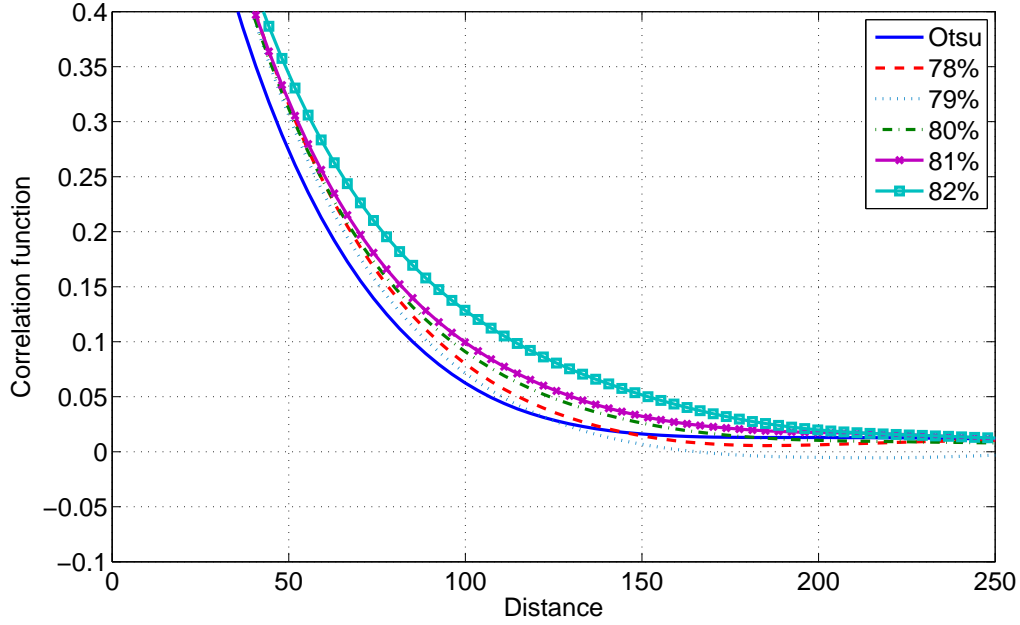
Figure 5.1.4.: Correlation function of Bentheimer model upon rescaling the sizes of the grains; the correlation function shown is zoomed at the region, where the difference between the curves is greatest.

Figure 5.1.3 shows the correlation function of the models from Table 5.1 compared with the Bentheimer sample thresholded by Otsu's method (Sec. 3.2.2). Fig. 5.1.4 shows the same data from Fig. 5.1.3, but zoomed into the region with the greatest difference between the curves. We find that upon decreasing the rescale ratio for the grains, the correlation function tends faster to zero, except the 78% measurement; which, peculiarly, lies between 79% and 80%. This can be obviously seen in Fig. 5.1.4, at the distance range between $100\,\mu\mathrm{m}$ and $150\,\mu\mathrm{m}$.

5.1.2. Grain orientation ranges

Seven samples were created with different *orientation ranges* starting from 0 degrees (no orientation), up to from -90 to 90 degrees [4, 3, 31]. In every model, the grains are allowed to rotate three times from $-\theta$ to θ, where θ is any angle of the Euler angles. Table 5.2 shows a comparison between the Minkowski functionals of those models compared with the thresholded sample labeled "Otsu" (Sec. 4.2). Fig. 5.1.5 is a plot for the table's values.

	Otsu	0°	15°	30°	45°	60°	75°	90°
Porosity	0.21	0.187	0.190	0.198	0.207	0.213	0.216	0.214
Specific surface (mm^{-1})	17.38	13.23	13.36	13.56	13.72	13.84	13.87	13.76
Mean curvature (mm^{-1})	298	115	117	117.2	112.4	108	106.4	106.6
Total curvature (mm^{-1})	-16154	-3541	-3419	-3027	-2783	-2600	-2937	-2947

Table 5.2.: Comparison between seven built samples with different orientation angles' ranges. Minkowski functionals of the models are compared with the Bentheimer sample thresholded with Otsu's method (Sec. 3.2.2).
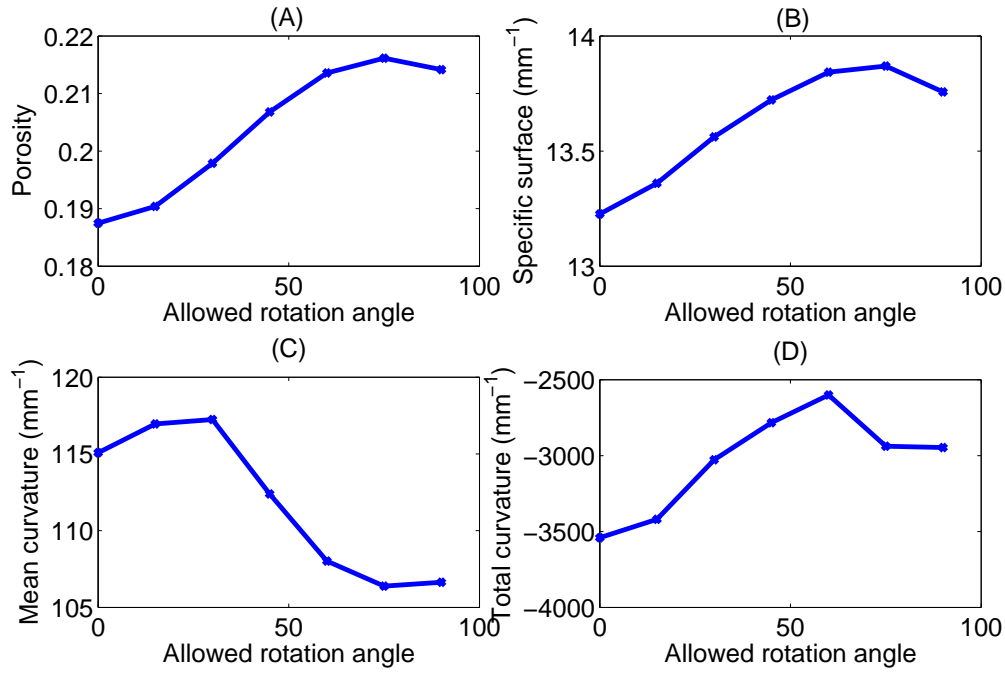

Figure 5.1.5.: The effect of changing the maximum allowed orientation angle upon the Minkowski functionals. (A): effect upon porosity. (B): effect on specific surface. (C): effect on mean curvature. (D): effect on total curvature.

We can see from Table 5.2 and Fig. 5.1.5 that limiting the orientation of the grains causes a monotonic change up to some angle range, then the readings drop down after that angle range. For porosity and specific surface this angle is $75°$. This result can be explained for the porosity and specific surface by saying that the grains reach their maximum overlap at this angle.

Fig. 5.1.6 shows a comparison between local porosity distributions for different allowed orientations ranges for the grains. We find that changing this variable has no effect at all on the sharpness of the curve for the local porosity distribution.
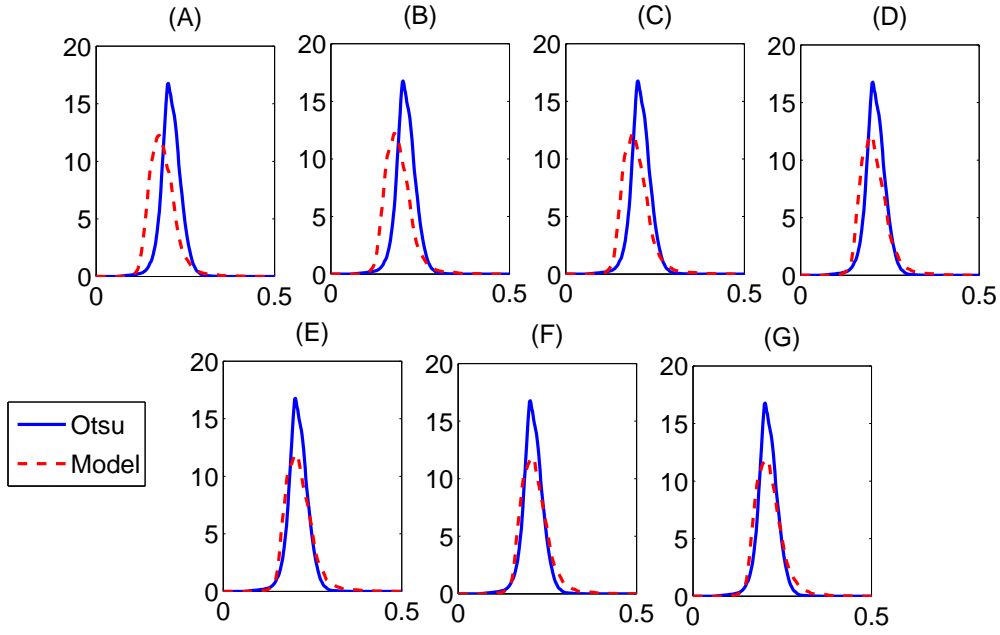
Figure 5.1.6.: Local porosity distribution as a function of porosity. The figure is a comparison between the local porosity distributions for different allowed angle orientations for the grains. A: $0°$. B: $15°$. C: $30°$. D: $45°$. E: $60°$. F: $75°$. G: $90°$. Every model's plot was done in an independent frame due to the closeness of the plots. If they were all put in one frame they would be indistinguishable.

We see from Fig. 5.1.6 that limiting the orientation angles does not affect the local porosity distribution at all; it barely affects it due to the slight change in porosity; i.e., shifting it, but not the sharpness of the curve (for sharpness definition, refer to the introduction of Sec. 5.1).

We conclude here that limiting orientation angles does not have a significant effect that can be exploited to control the microstructure's properties.

5.1.3. Grains overlap

Five different models were created with different *maximum allowed overlap* in deposition, ranging from 0.1 to 0.3 (overlap explained in Sec. 4.2). Table 5.3 shows a comparison between the Minkowski functionals of those models compared with the thresholded sample labeled "Otsu".

	Otsu	0.1	0.15	0.2	0.25	0.3
Porosity	0.21	0.193	0.195	0.217	0.229	0.236
Specific surface (mm^{-1})	17.38	13.53	13.21	13.08	12.76	12.15
Mean curvature (mm^{-1})	298	126.6	118.9	103.9	92.2	82.1
Total curvature (mm^{-1})	-16154	-3003	-2402	-1550	-1194	-884

Table 5.3.: Comparison between five built models with different maximum overlap value. Values of the maximum overlaps are shown in the first raw. Minkowski functionals of the models are compared with the Bentheimer sample thresholded by Otsu's method (Sec. 3.2.2).

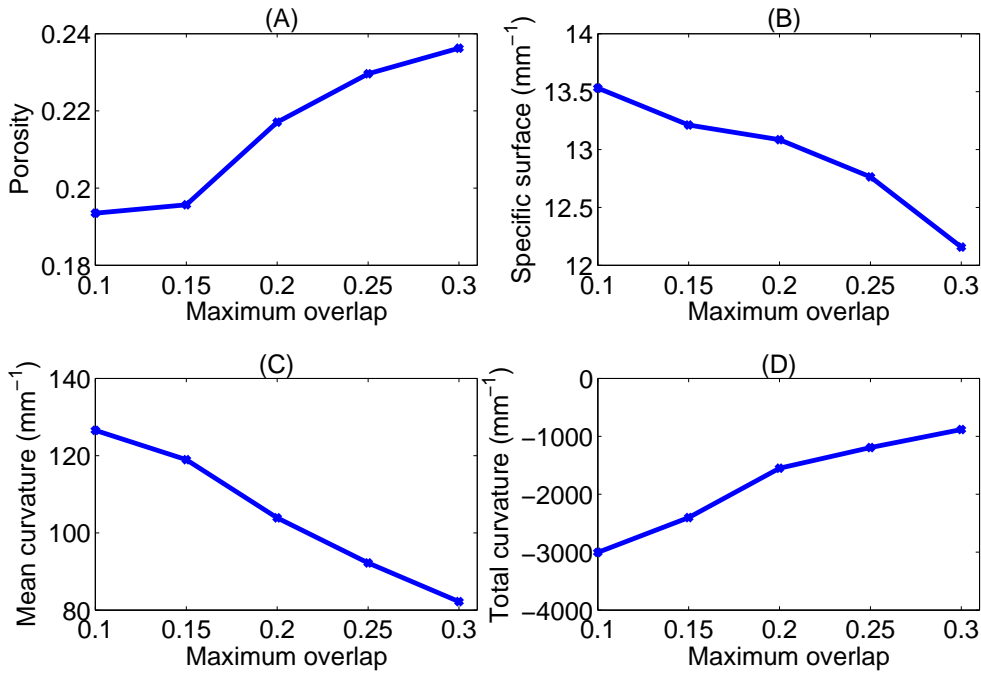Fig. 5.1.7 shows the previous table's plots.

Figure 5.1.7.: The effect of changing the maximum allowed overlap in deposition upon the Minkowski functionals. (A): effect upon porosity. (B): effect on specific surface. (C): effect on mean curvature. (D): effect on total curvature.

We see from Table 5.3 and Fig. 5.1.7 that overlap limit has a significant effect on Minkowski functionals, close to the effect we had of grain size distribution rescaling; more important, it is a monotone that can be exploited by tweaking it for getting specific characteristics for the model we want to build.

Fig. 5.1.8 shows a comparison between local porosity distributions for different maximum overlaps. We find that decreasing the overlap makes the porosity distribution sharper (sharpness definition could be found in the introduction of Sec. 5.1). This fact was a strong

motivation for devising the idea of minimizing the overlap (Sec. 4.3.2). The overlap minimization algorithm was done, because we wanted to get the sharpest possible local porosity distribution curve to fit the Bentheimer sample that is thresholded by Otsu's method.
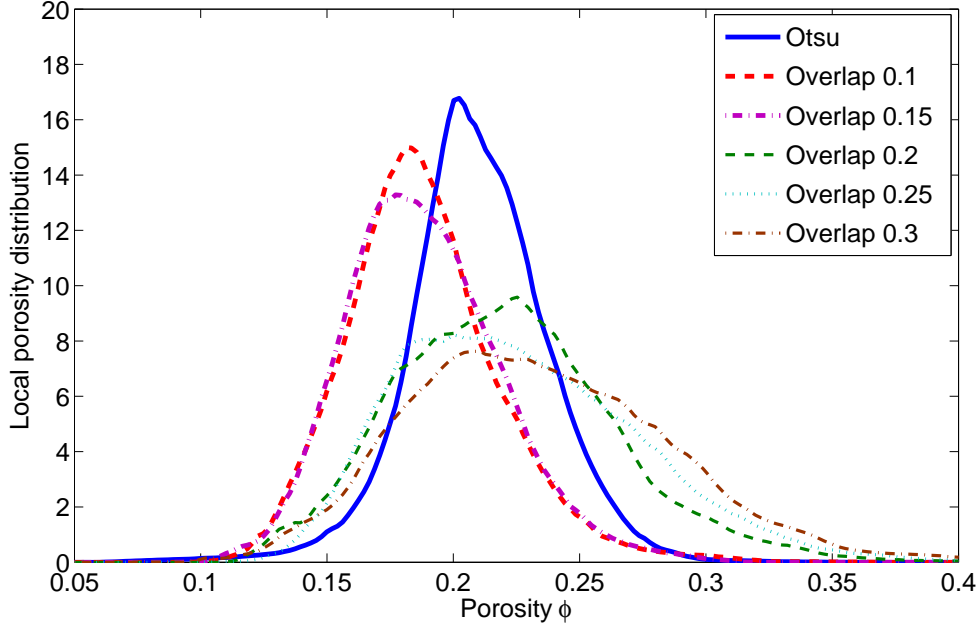

Figure 5.1.8.: Local porosity distribution as a function of porosity. The different curves represent the local porosity distribution for different maximum allowed overlap in the deposition process. The overlap value in the legend denotes the maximum allowed overlap in the deposition process.

5.1.4. Different decoration (different numbers of facets per polyhedron)

Six models were created with different decorations in this part; the same packing was used with different decorations. Each decoration is made up of grains that are polyhedra with different number of polyhedron's facets (discussed in Sec. 4.3.1). In the models created, we change the number of facets starting from 36 facets for the first model up to 121 facets for the last model. Table 5.2 shows Minkowski functionals measurements for the created models.

	Otsu	36	49	64	81	100	121
Porosity	0.21	0.150	0.168	0.199	0.204	0.218	0.226
Specific surface (mm^{-1})	17.38	10.99	11.7	12.96	13.08	13.6	13.8
Mean curvature (mm^{-1})	298	143.3	132.8	112.7	108.3	97.8	90.85
Total curvature (mm^{-1})	-16154	692	-471	-1745	-1939	-2597	-3155

Table 5.4.: Comparison between six built models with different numbers of facets per polyhedron. Minkowski functionals of the models are compared with the Bentheimer sample thresholded with Otsu's method (Sec. 3.2.2).

Fig. 5.1.9 shows plots for the data in Table 5.4.
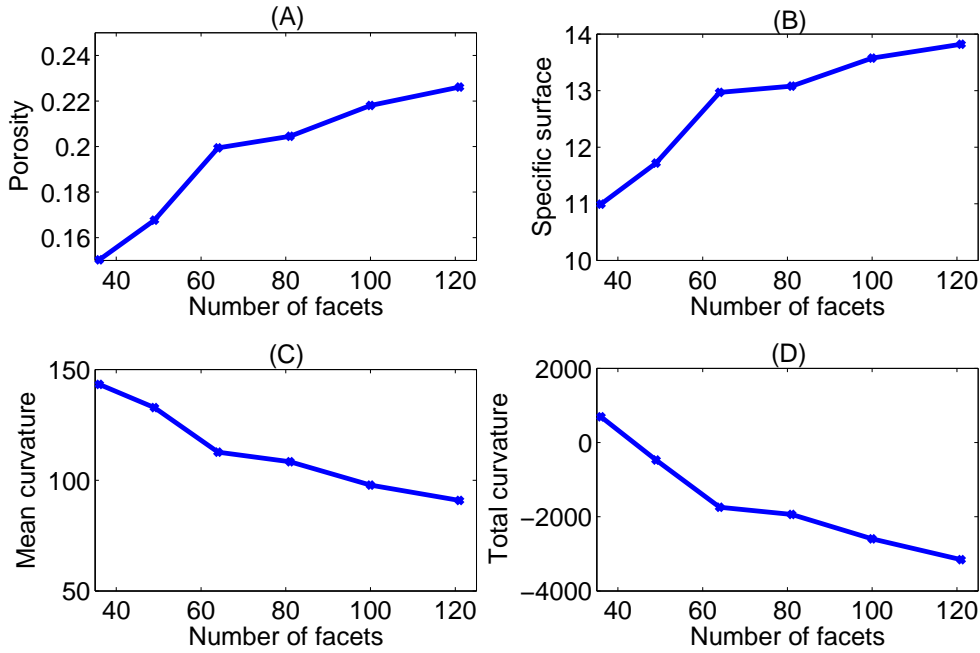
Figure 5.1.9.: The effect of changing the number of facets per polyhedron in decoration upon the Minkowski functionals. (A): effect upon porosity. (B): effect on specific surface. (C): effect on mean curvature. (D): effect on total curvature.

Another parameter with good monotonic effect on the Minkowski functionals. We see from Table 5.4 and Fig. 5.1.9 that changing the number of facets of the polyhedra in the model has almost a linear effect on Minkowski functionals. This indicates to the ability to exploit this parameter to tweak Minkowski functionals' values.

Fig. 5.1.6 shows a comparison between local porosity distributions for different decorations according to the number of facets per polyhedron.

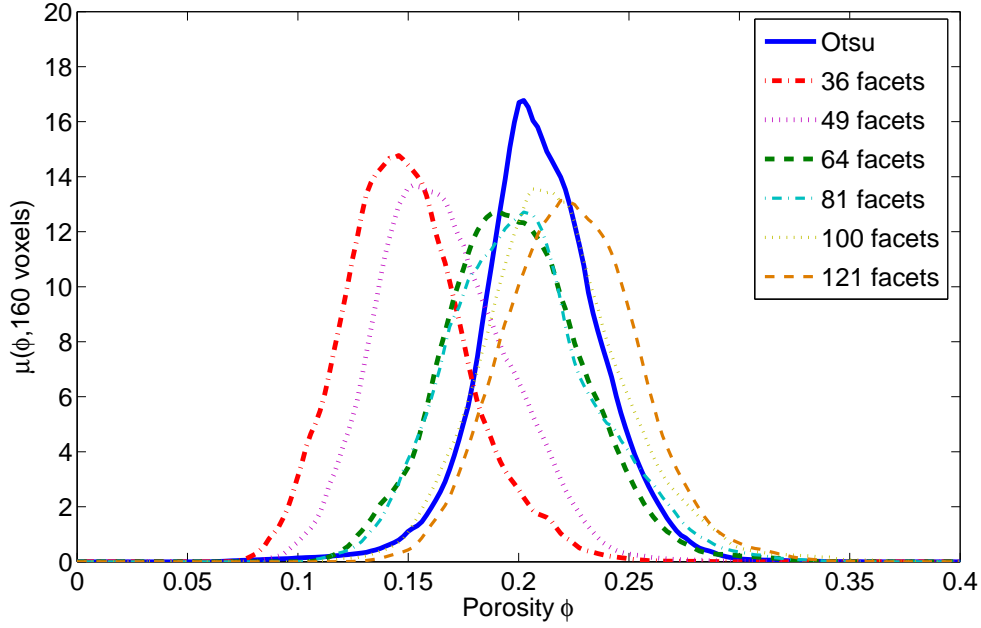Figure 5.1.10.: Local porosity distribution in different decorations, according to the number of facets per polyhedron.

We see from Fig. 5.1.10 that increasing the number of facets does not change the sharpness of the curve significantly, but only shifts it due to the reduction of the average grain volume; i.e., the change in porosity (for sharpness definition, refer to the introduction of Sec. 5.1).

This shows that changing the number of facets is a good parameter for controlling Minkowski functionals but not for local porosity distribution.

5.1.5. Different decorations (different elongation ratios for polyhedra)

Five models were created with different decorations in this section. In each decoration, the grains possess polyhedra with different maximum elongation ratios, starting from 0.2 maximum elongation ratio up to 1 (details on elongation mechanism was discussed in Sec. 4.3.1.2). All polyhedra used in all models consist of 121 facets. The following table shows Minkowski functionals measurements for the created samples.

	Otsu	0.2	0.4	0.6	0.8	1
Porosity	0.21	0.347605	0.311399	0.275495	0.239634	0.226107
Specific surface (mm^{-1})	17.38	17.1156	16.3308	15.4264	14.2611	13.8193
Mean curvature (mm^{-1})	298	-15.5866	18.9592	51.5261	81.1658	90.8505
Total curvature (mm^{-1})	-16154	-5793.89	-5573.38	-4792.12	-3188.99	-3155.24

Table 5.5.: Comparison between five built models with different maximum allowed elongation ratios per polyhedron. Minkowski functionals of the models are compared with the Bentheimer sample thresholded with Otsu's method (Sec. 3.2.2).

Fig. 5.1.11 shows the previous table's plots.
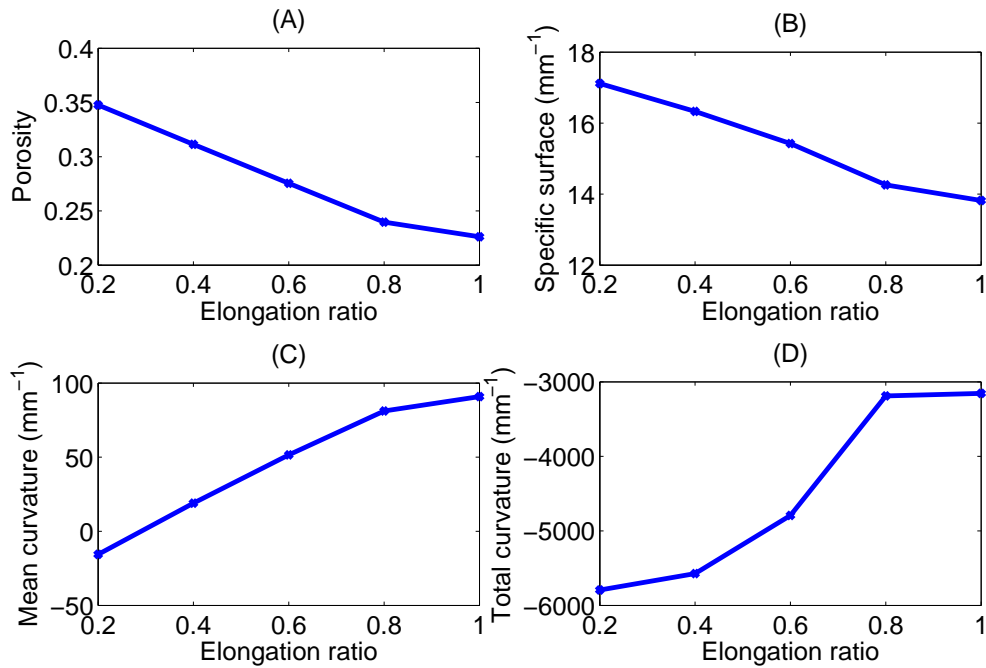
Figure 5.1.11.: The effect of changing the maximum elongation ratio of polyhedra upon the Minkowski functionals. (A): effect upon porosity. (B): effect on specific surface. (C): effect on mean curvature. (D): effect on total curvature.

From Table 5.5 and Fig. 5.1.11, we see that setting the maximum elongation ratio of the polyhedra has a very strong effect on porosity and specific surface; stronger than everything else we had so far. This does not mean we can deeply exploit this parameter, because this will affect the visual appearance of the model. Controlling porosity with this parameter is a bad move due to its high sensitivity to it, but for the specific surface it is good enough and feasible.

Fig. 5.1.6 shows a comparison between local porosity distributions for different decorations, according to the maximum elongation ratio of the polyhedra.
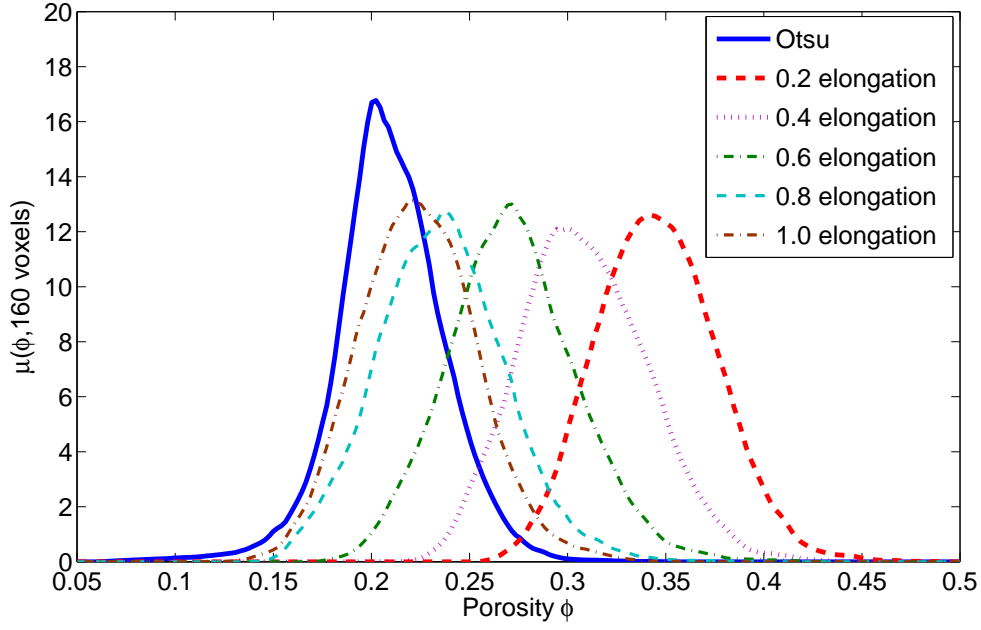
Figure 5.1.12.: Local porosity distribution for different decorations, i.e. maximum elongation ratio.

From Fig. 5.1.12 that elongation does not effect the sharpness of the local porosity distribution curves (for sharpness definition, read the introduction of Sec. 5.1). It merely shifts the curves due to the change in porosity which we find very high.

5.2. Conclusion

In this chapter, we investigated the tend of the microstructure characteristics as a function of the parameters we used to build the model. We can see that there are many different approaches and tweaks for reaching specific microstructure characteristics. The question lies, eventually, in how we are going to collect the different parameters together to get the model of Bentheimer we are looking for, not only qualitatively, but also quantitatively. Table 5.6 summarizes the capability of every input parameter in controlling microstructure characteristics.

	Size	Orientation	Overlap	Facets	Elongation
Porosity	Yes	No	Yes	Yes	No
Specific surface	Yes	No	Yes	Yes	Yes
Mean curvature	Yes	No	Yes	Yes	Yes
Total curvature	Yes	No	Yes	Yes	Yes
Local porosity distribution curve sharpness	No	No	Yes	No	No

Table 5.6.: The column titles are the following. Size: Grain size distribution rescaling. Orientation: Grain orientation limiting. Overlap: Grains overlap. Facets: Number of facets per polyhedron. Elongation: Maximum elongation ratio of polyhedra.

With this information we systematically started building models for Bentheimer and tried to match the experimental sample quantitatively and qualitatively. The next chapter discuss the best model we achieved.

6. Results and discussion

6.1. The best Bentheimer model

According to the information obtained in Chapter 5, we constructed a Bentheimer model that could best fit our model qualitatively and quantitatively. Almost 80 models were built, following the trend we had in the parameter study. The best choice was eventually narrowed the following model. Table 6.1 shows the parameters used to build the model.

Fig. 6.1.1 shows a qualitative comparison between the Bentheimer model we built and the μ-CT image thresholded by Otsu's method.

Quantity name	Quantity value
Sphere density in deposition	$556 \, \mathrm{spheres}/\mathrm{mm}^3$
Maximum overlap	0.1
Provided size distribution rescale ratio	70%
Overlap minimized (OM) (Sec. 4.3.2)	Yes
OM cell size	$500 \, \mu\mathrm{m}^3$
OM iterations per grain	5
OM iterations per cell	3
Orientation range	Not limited due to overlap minimizer
Number of facets per polyhedron	36
Facets maximum elongation ratio	0.4
Number of different polyhedra shapes in the model	512

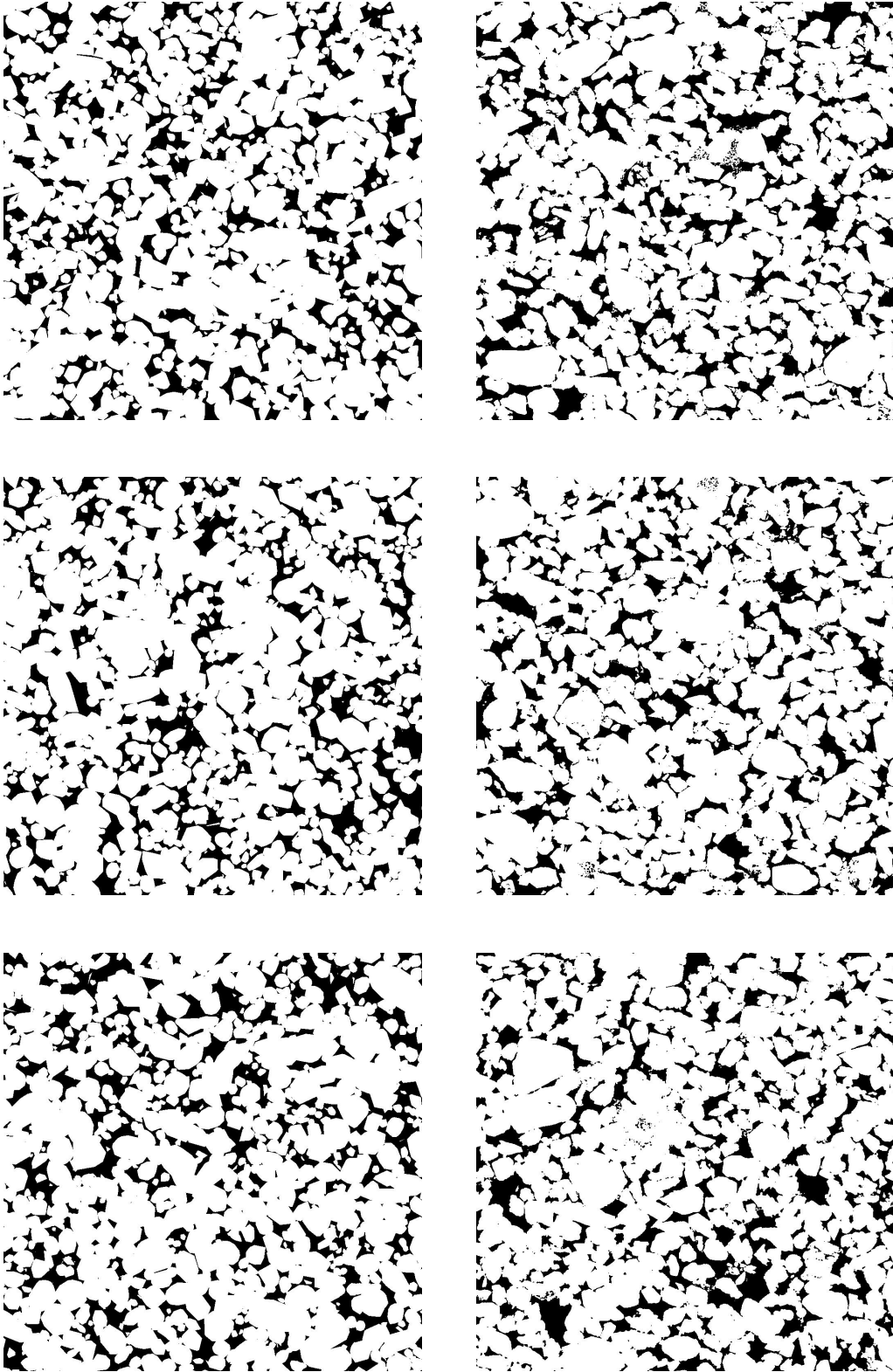Table 6.1.: The parameters used to build the Bentheimer model.

Figure 6.1.1.: Qualitative comparison between three random 2D slices from the synthetic μ-CT images of Bentheimer (left), and three random 2D slices from the experimental μ-CT images thresholded by Otsu's method (right). Details on thresholding the Bentheimer μ-CT is found in Sec. 3.2.2.

6.1.1. Geometrical characterization of the model

6.1.1.1. Minkowski functional

Table 6.2 shows a comparison of the Minkowski functionals between the model we built for Bentheimer and the Bentheimer sample thresholded by Otsu's method (Sec. 3.2.2). As we can see in Table 6.2, the porosity was achieved accurately, but the specific surface was almost close to the lowest value we obtained by the different thresholds we applied on the Bentheimer model. We can explain the high specific surface of the Bentheimer's experimental sample by the fact that thresholding the μ-CT image caused many undetermined regions to appear; i.e., increased the number of spurts in the thresholded image, which in role causes relatively more surface area than the expected value. The mean curvature and total curvature in Table 3.1 are not monotones and are not determined since they have a long range of fluctuations; nevertheless, we got values for them in our model that are within the values we obtained with maximum and minimum thresholds (can be seen as error bars).

	Model	Otsu	Minimum value	Maximum value
Porosity	0.21643	0.21468	0.17834	0.245018
Specific surface	15.6476	17.3802	15.7435	19.1452
Mean curvature	138.101	298.743	114.656	318.307
Total curvature	-4194.72	-16154.4	-21554	9402.64

Table 6.2.: Comparison of Minkowski functionals between the model and the Bentheimer sample thresholded by Otsu's method. The last two columns are the minimum and maximum of different thresholds from Table 3.1.

6.1.1.2. Local porosity distribution

The local porosity distribution was measured in the model for the same cell sizes used for the Bentheimer sample (Sec. 3.2.2.3). Fig. 6.1.2 shows the local porosity distribution at different measurement cells' sizes. Comparing Fig. 3.2.8 and 6.1.2, we find that they strongly agree; nevertheless, we find the strange double peak for the largest length-scale, which is a problem of homogeneity, and cannot be fixed with the currently available technology; we used the overlap minimizer to fix a part of the homogeneity problem.
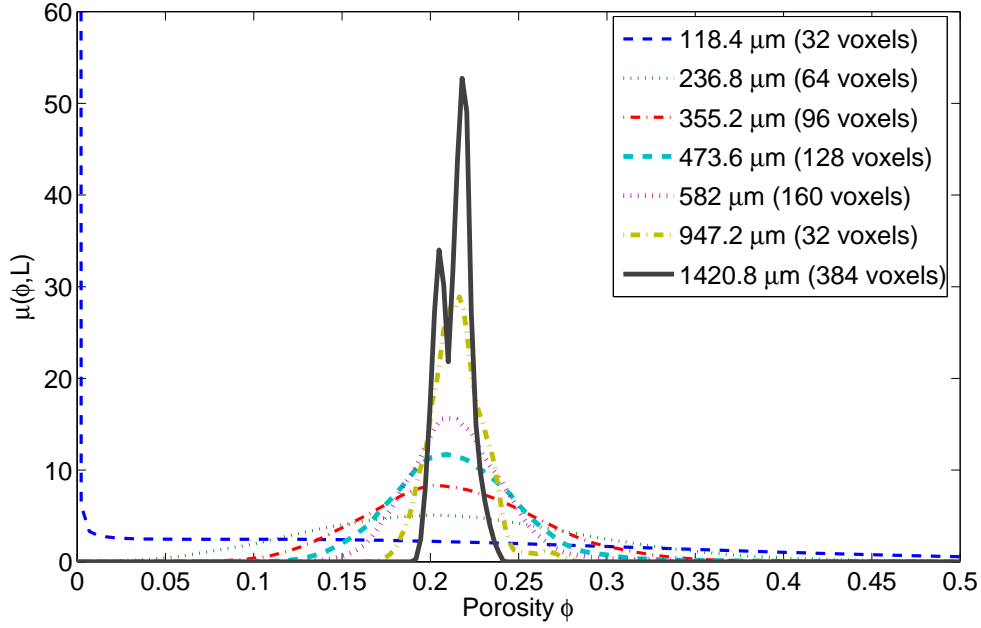
Figure 6.1.2.: Local porosity distribution of the Bentheimer model. The cells of measurement are cubes with the side-length mentioned in the legend of the graph. We find a peculiar peak at the cell size 384 voxels. This peak means that at this cell size different porosity is found at different regions, which means the model has a problem with homogeneity at this length scale. We believe that this problem is due to the formation of clusters of highly packed grains in some regions that lower the porosity. Such a problem cannot be solved using spheres deposition algorithm, and needs a better technique for lowering the overlap for the grains themselves.

The local porosity distribution of the model was compared with the Bentheimer μ-CT images that are thresholded with Otsu's method (details on thresholding in Sec. 3.2.2) for better comparison. Fig. 6.1.3 shows this comparison.
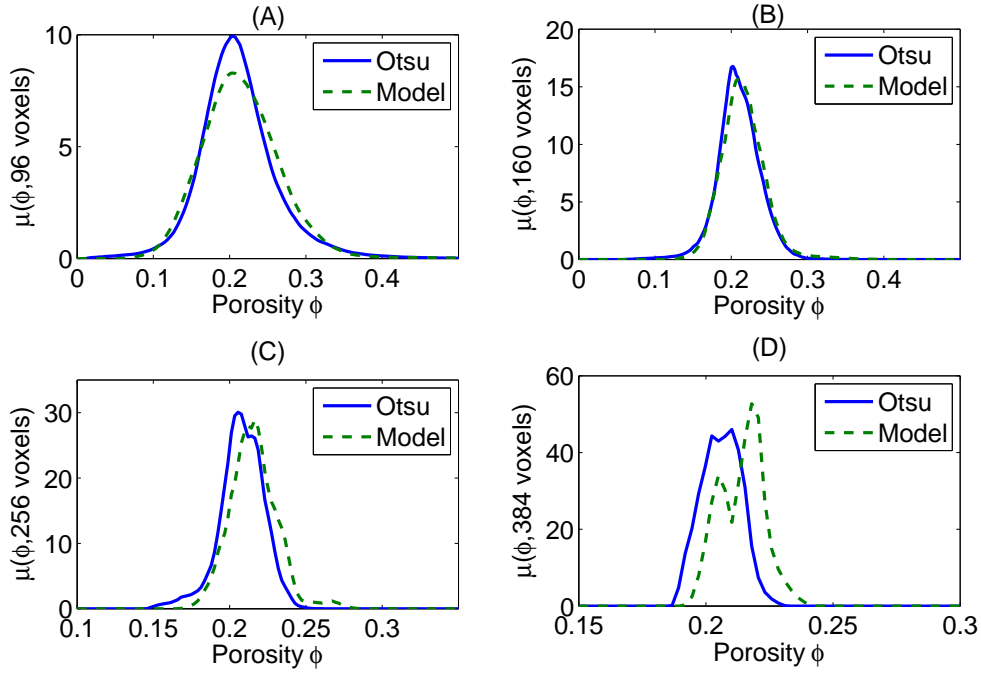
Figure 6.1.3.: Comparison between the local porosity distribution of the Bentheimer model and the Bentheimer sample thresholded by Otsu's method (Sec. 3.2.2). The measurement cells are cubes with the following side-lengths. (A): $335.2\,\mu m$ (96 voxels). (B): $592\,\mu m$ (160 voxels). (C): $947.2\,\mu m$ (256 voxels). (D) $1420.8\,\mu m$ (384 voxels).

6.1.1.3. Local percolation probabilities

The local percolation probabilities were measured for the model with the same cells' sizes we had for the experimental Bentheimer sample (Sec. 3.2.2). Fig. 6.1.4 shows the local percolation probabilities for the Bentheimer model. Comparing 3.2.10 and 6.1.4, we find a good agreement between them. A grid was inserted for better comparison.
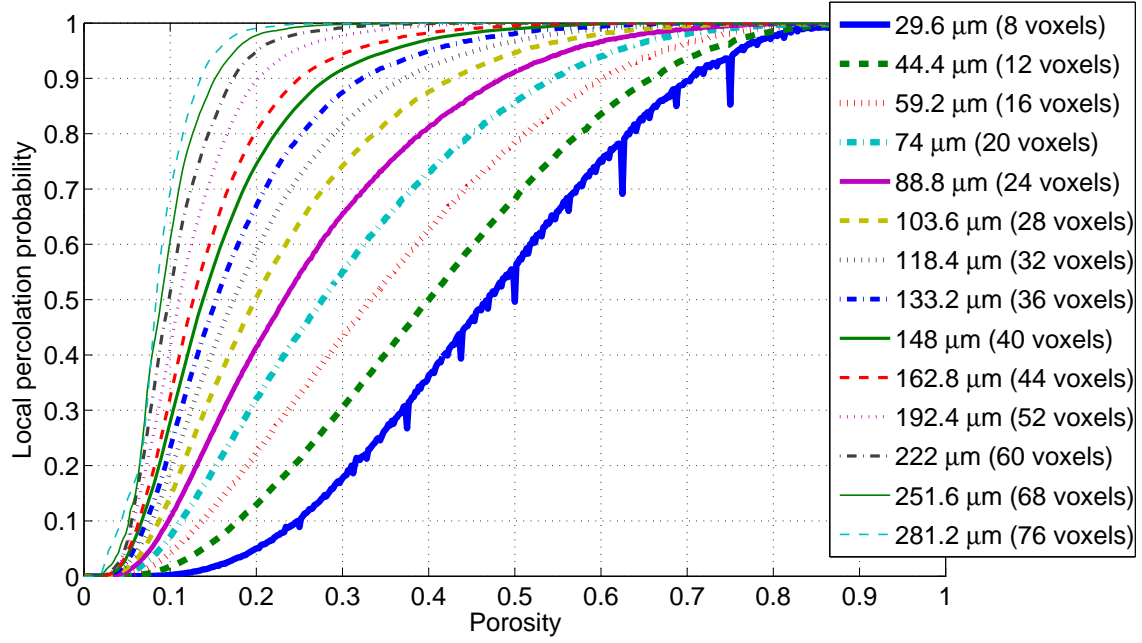
Figure 6.1.4.: Local percolation probability of the Bentheimer model different measurement cell sizes. The measurement cell is a cube, the scales mentioned in the legend are the side-length of the measurement cube.

Direct comparisons between the local percolation probabilities was done for few side-lengths. Fig. 6.1.5 shows this comparison.

We see that local percolation probabilities match between the model and the sample quite good at intermediate length scales. The difference found in the small length scales is due to the insufficient image resolution problems of the experimental μ-CT images, where it is difficult to match small (relative to the resolution) microstructure details due to the lack of information. The slight mismatch in big length scales is a surprise and could not be understood. Further investigation after larger length scales was, unfortunately, not possible due to the lack of equipments and the very long time it needs if the current equipments are used.
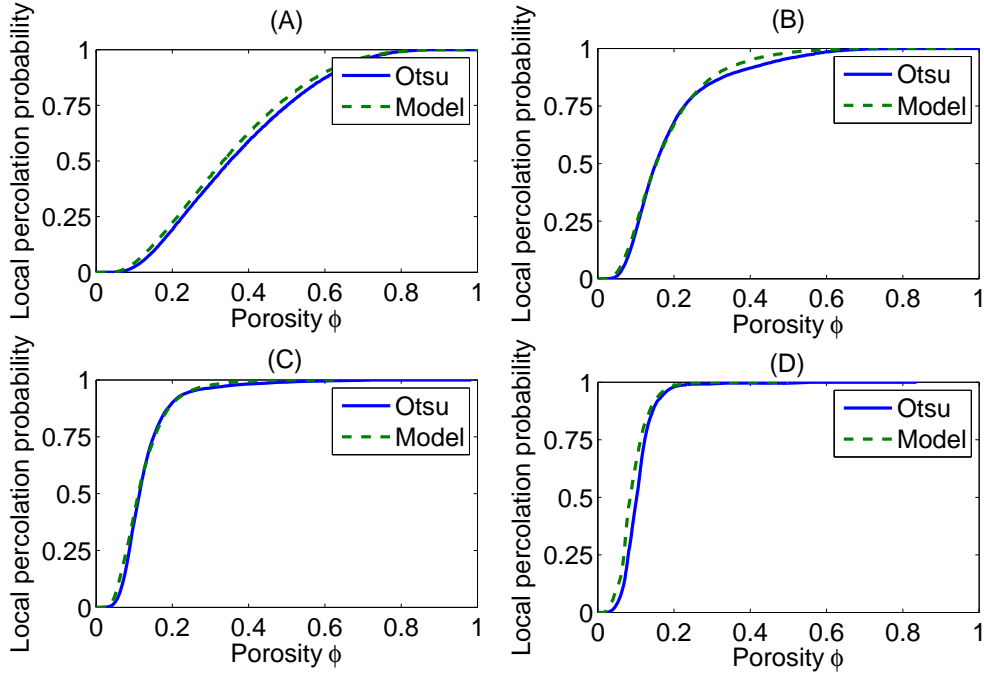
Figure 6.1.5.: Comparison between the local percolation probabilities of the experimental Bentheimer sample and the synthetic Bentheimer model with different measurement cell sizes. The measurement cells are cubes and the following mentioned sizes are in means of their side-lengths. The cells sizes are $59.2\,\mu\mathrm{m}$ (16 voxels) for (A). $133.2\,\mu\mathrm{m}$ (36 voxels) for (B). $192.4\,\mu\mathrm{m}$ (52 voxels) for (C). $266.4\,\mu\mathrm{m}$ (72 voxels) for (D).

6.1.1.4. Fraction of percolating cells

Using the data from Sec. 6.1.1.3, we performed the calculation of the local fraction of percolating cells. Confirming what is said in Sec. 6.1.1.3, we find that the best match is found in intermediate length scales, and as we formerly have said, we could not do further investigation due to the lack of equipments.
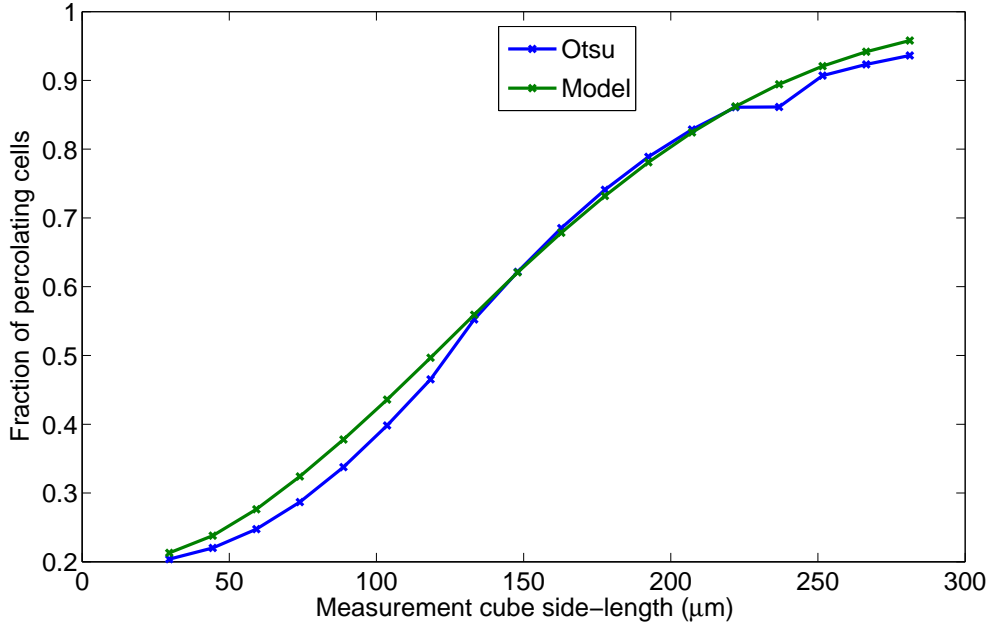
Figure 6.1.6.: Local fraction of percolating cells for the Bentheimer sample thresholded by Otsu's method compared with the model we created for Bentheimer.

6.1.2. Transport properties of the model

Table 6.3 shows a comparison between the quantitative transport properties of Bentheimer sample that is thresholded using Otsu's method (details on thresholding is in Sec. 3.2.2) and the model we have created. The transport properties were measured using a Lattice Boltzmann simulation and Darcy's law [34].

Attribute	Value for sample	Value for model
Average velocity in z-direction	$1.34 \times 10^{-3}\,\mathrm{\mu m/s}$	$1.26 \times 10^{-3}\,\mathrm{\mu m/s}$
Variance of velocity in z-direction	$7.25 \times 10^{-6}\,\mathrm{\mu m/s}$	$6.17 \times 10^{-6}\,\mathrm{\mu m/s}$
Min-Max velocity in z-direction	$[-3.43, 1.82] \times 10^{-2}\,\mathrm{\mu m/s}$	$[-2.89, 1.49] \times 10^{-2}\,\mathrm{\mu m/s}$
Dynamic viscosity	$0.0264\,\mathrm{kg/s\cdot\mu m}$	$0.0264\,\mathrm{kg/s\cdot\mu m}$
Global pressure gradient	$-4.31 \times 10^{-5}\,\mathrm{kg/s\cdot\mu m^2}$	$-4.33 \times 10^{-5}\,\mathrm{kg/s\cdot\mu m^2}$
Permeability	$3.074\,D$	$2.872\,D$

Table 6.3.: Lattice Boltzmann simulation results for Bentheimer sample thresholded by Otsu's method.

6.2. Conclusion

Using the tend we learned in Chapter 5, we created a model for Bentheimer that matches the real sample both qualitatively and quantitatively. The sample and the model matched at a wide length scale range. The transport properties of the model and the sample agreed up to some point after the agreement achieved in the microstructure's characteristics. This means that the microstructure's characteristics describe the samples, we are using, very well.

7. Conclusion and Outlook

This thesis discusses the characterization and modeling of a one-phase porous medium. The main purpose to such analysis is the big trouble in storing and analyzing the experimental μ-CT images.

The idea starts with defining a porous medium from a mathematical point of view. Then defining the important physical quantities in a porous medium (porosity, specific surface, etc), and the means to characterize different porous media's micro-structure in different length scales (local porosity theory).

The modeling process exempted us from using the pixel-wise imaging and reduced the problem to storing objects with their attributes in the continuum. It, also, made obtaining different synthetic μ-CT images relatively easy, rather than it being costly like it is in experimental μ-CT.

One phase of the Bentheimer sandstone was modeled successfully ignoring other two phases. They were ignored due to their very low volume fractions ($<1\%$), and due to their very weak effect on the microstructure's properties. We used the Hoshen-Kopelman algorithm to get the best segmentation possible for the phases of the experimental sample.

The standard modeling procedure did not suffice; an overlap minimization algorithm was devised in order to solve the problem of having elongated objects decorating spheres. The algorithm gave a more realistic scheme for the existence of packed anisotropic objects together to have a homogeneous overlap, and lowered the number of objects needed to achieve a certain porosity. The overlap minimization algorithm may be avoided in future modeling by using an ellipsoids' deposition algorithm rather than spheres.

We could achieve the model of Bentheimer by what we have learned in Chapter 5, where we understood the tend of the microstructure's characteristics as a function of the modeling parameters.

The geometrical, and consequently, the physical transport characteristics of the model and the original sample agree up to a very good level in a pretty wide length-scale range; nevertheless, some characteristics were not achieved good enough, like the specific surface, due to the poor quality of the μ-CT images available; i.e. lack of information.

A laboratory-size cubic model with side-length $2.4\,\mathrm{cm}$ was created, with the same parameters from Table 6.1. Creating bigger models is never a problem anymore with this modeling procedure.

A. Appendix

A.1. The Hoshen-Kopelman algorithm

The purpose of the Hoshen-Kopelman's algorithm is labeling clusters on a binary grid. A binary grid is a grid that contains only ones and zero. Fig. A.1.1 shows a 2D binary grid where we will apply the Hoshen-Kopelman algorithm, as an example.

1	0	1	1	0	0	1	1	1	1	1	1	1	1	0
0	0	1	0	0	1	0	0	1	1	1	0	0	0	1
0	1	1	1	1	0	0	0	0	1	0	1	1	1	1
1	0	1	1	0	1	0	0	0	0	1	1	0	0	1
0	0	1	1	0	0	0	0	1	0	0	0	1	0	1
1	0	1	0	1	0	0	0	1	0	0	1	0	1	1
1	1	0	0	1	0	1	1	1	1	1	1	1	1	0
1	0	0	1	1	1	0	0	1	1	1	0	0	1	1
1	1	0	1	1	1	0	1	0	1	0	0	1	0	0
0	0	1	0	0	1	1	0	1	1	0	0	1	0	0

Figure A.1.1.: A binary grid. We can see that it contains only the values ones and zeros, as it is the case in a thresholded image.

The Hoshen-Kopelman algorithm is an algorithm that consists of a systematic scan for the cells in a 2D grid. The scan goes, presumably, from top left, down to the bottom right of the image. The algorithm checks every cell whether its value is 0 or 1. If the value of the current cell is 0, the cell is skipped. Otherwise, the cell on the left and the cell above are checked for their values. If one of these two neighboring cells has the value 1, we assign the current cell the same label of the neighboring cell with the value 1. Otherwise, if both have the value 1, a union operation is done to place the neighboring cells in one cluster. The pseudo-code in Algorithm A.1 summarizes the Hoshen-Kopelman algorithm in its simplest form.

Algorithm A.1 A pseudo-code for the Hoshen-Kopelman algorithm. The algorithm is a little bit modified than the original algorithm given in [26].

```
for(y from 0 to num_of_rows)
        for(x from 0 to num_of_columns)
        {
                if( cell[x,y] == 1)
                {
                        if(x == 0)
                                left = 0;
                        else
                                left = cell[x-1,y];
                        if(y == 0)
                                above = 0;
                        else
                                above = cell[x,y-1];

                        if(left == 1 && above == 1)
                                union(cell[x,y],cell[x-1,y],cell[x,y-1]);
                        else if(left == 1 && above == 0)
                                union(cell[x,y],cell[x-1,y]);
                        else if(left == 0 && above == 1)
                                union(cell[x,y],cell[x,y-1]);
                        else if(left == 0 && above == 0);
                                new_cluster(cell[x,y]);
                }
        }
```

Fig. A.1.2 shows the result of applying the Hoshen-Kopelman algorithm upon the grid shown in Fig. A.1.1.

Figure A.1.2.: The result of applying the Hoshen-Kopelman algorithm on the grid in Fig. A.1.1. Contiguous clusters are labeled. Colors are there to make the visual appearance more understandable.

The way we use the Hoshen-Kopelman algorithm is pretty different. We do not, actually,

care about the clusters' labels; we care about the amount of cells they contain; therefore, after applying the Hoshen-Kopelman algorithm, we do not save them as they look in A.1.2, but save them, again, as a binary image. Into this binary image, we pass only the clusters that contain an amount of cells greater than a specific amount k that we specify. We call k the *cluster-size threshold*. For example, in Fig. A.1.2, if we define the cluster-size threshold as $k = 10$, the result will be as it is shown in Fig. A.1.3. In Fig. A.1.3, we notice that every cluster that contained a number of cells ≤ 10 is removed.

0	0	1	1	0	0	1	1	1	1	1	1	1	1	0
0	0	1	0	0	0	0	0	1	1	1	0	0	0	1
0	1	1	1	1	0	0	0	0	1	0	1	1	1	1
0	0	1	1	0	0	0	0	0	0	1	1	0	0	1
0	0	1	1	0	0	0	0	1	0	0	0	0	0	1
0	0	1	0	0	0	0	0	1	0	0	1	0	1	1
0	0	0	0	0	0	1	1	1	1	1	1	1	1	0
0	0	0	0	0	0	0	0	1	1	1	0	0	1	1
0	0	0	0	0	0	0	0	0	0	1	0	0	0	0
0	0	0	0	0	0	0	0	1	1	0	0	0	0	0

Figure A.1.3.: This figure represents Fig. A.1.2 after applying cluster-size threshold $k = 10$. We see that all clusters in Fig. A.1.2 that contain ≤ 10 cells are removed.

Since our sample is 3D, a 3D Hoshen-Kopelman algorithm was used. Three directions (x, y, z) were checked around every cell, rather than two as it is in the standard Hoshen-Kopelman algorithm; i.e., in addition to the cells to the left and above, we check, also, the cell that has the same coordinates of the current cell but in the previous image slice. We, also, changed the standard algorithm by defining what we have called a *sliding-window* to ensure that long connected rims would not be taken as clusters. Sliding window means that we define an integer number n, that we call *window size*, that specifies how many image slices to apply the Hoshen-Kopelman algorithm upon, before flushing the cluster information and starting over with the next n image slices, where the next window of image slices differ by the previous one by shifting the previous set of image slices by 1 (Fig. A.1.4). For example, for $n = 5$ (as was chosen for the sample), if the process starts with image slice number 0, the set of image slices to apply the Hoshen-Kopelman algorithm upon are

$$
\begin{aligned}
0 &\rightarrow 4 \\
1 &\rightarrow 5 \\
2 &\rightarrow 6 \\
3 &\rightarrow 7 \\
\vdots \quad &\vdots \quad \ddots
\end{aligned}
$$

Why do we do this? In the first place, the purpose of applying the Hoshen-Kopelman

algorithm is separating the fillings from the rims of the normal grains (Sec. 3.2.2). If we apply the algorithm on the whole set of image slices, the rims may form connected clusters along the whole set of image slices, and their sizes (cluster sizes caused by contiguous rims cells) would be comparable to the size of the fillings. To avoid this happening, we use the concept of a sliding window, and reset the cluster label information after every n image slices, where the fillings could form clusters containing cells greater than the cluster-size threshold, but the connected rims' cells could not. Fig. A.1.4 shows the concept of a applying a sliding window on the Hoshen-Kopelman algorithm upon the image slices labeled with the numbers. In Fig. A.1.4, (A), we see 10 image slices that we want to apply the 3D Hoshen-Kopelman algorithm upon. (B) shows the Hoshen-Kopelman algorithm being applied with a sliding window, the window size is $n = 5$. After applying the Hoshen-Kopelman algorithm on the first five image slices, we save the result into binary image slices, and move to the next step (C) and continue saving the output into the same binary image slices, but add a new slice in every step, since there are $n - 1$ common image slices between every two subsequent steps. The output binary image slices keep growing at every step by "1" (except the first step, where it saves the whole window size). To solve the conflict problem between the common image slices (already saved ones and the ones to be saved), the results of every step, that we get using a sliding window, are saved to the output image slices using an OR gate. Meaning, that the pixels that have the value 1 always overwrite the pixels in the saved binary image slices.

(A) | 0 | 1 | 2 | 3 | 4 | 5 | 6 | 7 | 8 | 9 |

(B) | 0 | 1 | 2 | 3 | 4 | 5 | 6 | 7 | 8 | 9 |

(C) | 0 | 1 | 2 | 3 | 4 | 5 | 6 | 7 | 8 | 9 |

(D) | 0 | 1 | 2 | 3 | 4 | 5 | 6 | 7 | 8 | 9 |
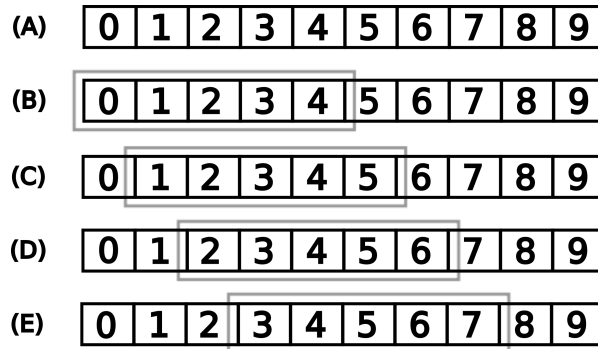
(E) | 0 | 1 | 2 | 3 | 4 | 5 | 6 | 7 | 8 | 9 |

Figure A.1.4.: The concept of a "sliding window". (A): Ten 2D image slices that we want to apply the 3D Hoshen-Kopelman algorithm upon. (B): Starting the Hoshen-Kopelman algorithm with a sliding window, the size of the window is $n = 5$ (the window is represented by the gray rectangle). After applying the Hoshen-Kopelman algorithm on the first five image slices, we save the result into binary image slices, and move to the next step (C). (C): The second step in a sliding window algorithm. We see that the window has shifted by a single image slice. The process continues after (C) by (D) and (E), etc. The results of every step, that we get using a sliding window, are saved to the output file using an OR gate; meaning, that pixels that have the value 1 always overwrite the pixels in the saved binary image slices.

Bibliography

[1] J. Bear and Y. Bachmat. Transport in Porous Media 1, volume 1, chapter Macroscopic Modelling of Transport Phenomena in Porous Media. 1: The Continuum Approach, pages 213–240. D. Reidel Publishing Company, 1986. 9

[2] J. Bear and Y. Bachmat. Introduction to modeling of transport phenomena in porous media. Springer, 1990, ISBN: 978-0-792-31106-5. 4, 9

[3] B. Biswal, R. J. Held, V. Khanna, J. Wang, and R. Hilfer. Towards precise prediction of transport properties from synthetic computer tomography of reconstructed porous media. *Phys. Rev. E*, **80**(4):041301, Oct 2009. 1, 30, 31, 33, 39, 45, 50

[4] B. Biswal, P. Oren, R. Held, S. Bakke, and R. Hilfer. Modeling of multiscale porous media. *Image Anal Stereol*, **28**:23–34, 2009. 30, 31, 32, 33, 34, 39, 50

[5] B. Biswal, P.-E. Øren, R. J. Held, S. Bakke, and R. Hilfer. Stochastic multiscale model for carbonate rocks. *Phys. Rev. E*, **75**(6):061303, Jun 2007. 18

[6] F. Boger, J. Feder, T. Jossang, and R. Hilfer. Microstructural sensitivity of local porosity distributions. *Physica A: Statistical Mechanics and its Applications*, **187**(1-2):55 − 70, 1992. 10

[7] G. Choquet. Theory of capacities, volume 5. Ann. l'institut Fourier, 1953, ISSN: 0373-0956. 6

[8] Dullien. Porous Media Fluid Transport and Pore Structure. Academic Press, second edition, 1992, ISBN: 978-0-122-23651-8.

[9] A. El Bied, J. Sulem, and F. Martineau. Microstructure of shear zones in fontainebleau sandstone. *International Journal of Rock Mechanics & Mining Sciences*, **39**:917–932, Jun 2002. 1, 26

[10] W. Feller. An Introduction to Probability Theory and Its Applications, volume 1. Wiley, 3rd edition, 1968, ISBN: 978-0-471-25708-0. 6, 10

[11] W. Feller. An Introduction to Probability Theory and Its Applications, volume 2. Wiley, 2nd edition, 1971, ISBN: 978-0-471-25709-7. 6, 10

[12] Rafael C. Gonzalez and Richard E. Woods. Digital Image Processing (3rd Edition). Prentice-Hall, Inc., Upper Saddle River, NJ, USA, 3rd edition, 2008, ISBN: 978-0-131-68728-8. 18, 20, 22

[13] J. Hertz. Disordered systems. *Physica Scripta*, **1985**(T10):1, 1985. 1

[14] R. Hilfer. Geometric and dielectric characterization of porous media. *Phys. Rev. B*, **44**(1):60–75, Jul 1991. 10

[15] R. Hilfer. Geometry, dielectric response and scaling in porous media. *Physica Scripta*, **1992**(T44):51, 1992. 10

[16] R. Hilfer. Local-porosity theory for flow in porous media. *Phys. Rev. B*, **45**(13):7115–7121, Apr 1992. 10

[17] R. Hilfer. Classification theory for anequilibrium phase transitions. *Phys. Rev. E*, **48**(4):2466–2475, Oct 1993. 7

[18] R. Hilfer. Classification theory for phase transitions. *International Journal of Modern Physics B*, **7**(26):4371–4387, 1993. 7

[19] R. Hilfer. Random magnetism high-temperature superconductivity, chapter On a new class of phase transitions, pages 85–99. World scientific publishing Co. Pte. Ltd., 1993. 7

[20] R. Hilfer. Absence of hyperscaling violations for phase transitions with positive specific heat exponents. *Z. Phys. B*, **96**:63, 1994. 10

[21] R. Hilfer. Fractional master equations and fractal time random walks. *Phys. Rev. E*, **51**(2):R848–R851, 2 1995. 7

[22] R. Hilfer. Statistical Physics and Spatial Statistics, volume 554/2000, chapter Local Porosity Theory and Stochastic Reconstruction for Porous Media, pages 203–241. Springer Berlin / Heidelberg, 2000.

[23] R. Hilfer. Local porosity theory for electrical and hydrodynamical transport through porous media. *Physica A*, **194**(1-4):406 – 414, 2002. 10

[24] R. Hilfer. Advances in Chemical Physics, chapter Transport and Relaxation Phenomena in Porous Media, pages 299–424. John Wiley & Sons, Inc, 2007. 1, 3, 4, 5, 6, 7, 8, 9, 10, 11, 12, 13

[25] R. Hilfer, B. NÃžst, E. Haslund, Th. Kautzsch, B. Virgin, and B. D. Hansen. Local porosity theory for the frequency dependent dielectric function of porous rocks and polymer blends. *Physica A*, **207**(1-3):19 – 27, 1994. 10

[26] J. Hoshen and R. Kopelman. Percolation and cluster distribution. i. cluster multiple labeling technique and critical concentration algorithm. *Phys. Rev. B*, **14**(8):3438–3445, Oct 1976. 20, 71

[27] F. Jerry Lucia. Carbonate Resevoir Characterization. Springer, 1999, ISBN: 978-3-540-63782-0.

[28] D. Kendall. Stochastic geometry. Wiley, 1974. 6

[29] R. Kuehn. Gibbs vs. non-gibbs in the equlibrium ensemble approach to disordered systems. *Markov Process. Relat. Fields*, **10**(3):523–545, 2004. 1

[30] C. Lang, J. Ohser, and R. Hilfer. On the analysis of spatial binary images. *Journal of Microscopy*, **203**:303–313, 05 2001. 23

[31] F. Latief, B. Biswal, U. Fauzi, and R. Hilfer. Continuum reconstruction of the pore scale microstructure for fontainebleau sandstone. *Physica A*, **389**:1607–1618, May 2009. 1, 30, 31, 32, 33, 34, 39, 43, 44, 45, 50

[32] C. Manwart. Geometrische Modellierung und Transporteigenschaften poroeser Medien. PhD thesis, Universitaet Stuttgart, 2001. 13

[33] G. Matheron. Random sets and integral geometry. Wiley, 1975, ISBN: 978-0-471-57621-1. 6

[34] Ariel Narvaez, Thomas Zauner, Frank Raischel, Rudolf Hilfer, and Jens Harting. Quantitative analysis of numerical estimates for the permeability of porous media from lattice-boltzmann simulations. *Journal of Statistical Mechanics: Theory and Experiment*, **2010**(11):P11026, 2010. 13, 28, 67

[35] N. Otsu. A threshold selection method from gray-level histograms. *IEEE transactions on systems, man, and cybernetics*, **SMC**-**9**(1):62–66, 1979. 22

[36] P. K. Sahoo, S. Soltani, and A. K. C. Wong. A survey of thresholding techniques. *Computer Vision, Graphics, and Image Processing*, **41**(2):233 – 260, 1988. 22

[37] I. Saxl. Topics in disordered systems. *Applications of Mathematics*, **44**:244–244, 1999. 1

[38] W. Walter. Real and Complex Analysis. Mcgraw Hill, 1986, ISBN: 978-0-070-54234-1. 6

Acknowledgment

Hiermit versichere ich, dass ich die vorliegende Arbeit selbständige und nur mit den angegebenen Hilfsmitteln angefertigt habe und dass alle Stellen, die dem Wortlaut oder dem Sinne nach anderen Werken entnommen sind, durch Angabe der Quallen als Entlehnungen kenntlich gemacht werden sind.

_____

Samer Afach